Stability, energetics, and magnetic states of cobalt adatoms on graphene: An *ab initio* quantum Monte Carlo study

Yudistira Virgus

Palembang, South Sumatra, Indonesia

Master of Science, College of William and Mary, 2011
Bachelor of Arts, Institut Teknologi Bandung, 2008

A Dissertation presented to the Graduate Faculty
of the College of William and Mary in Candidacy for the Degree of
Doctor of Philosophy

Department of Physics

The College of William and Mary
August 2015

APPROVAL PAGE

This Dissertation is submitted in partial fulfillment of
the requirements for the degree of

Doctor of Philosophy

Yudistira Virgus

Approved by the Committee, May, 2015

Committee Chair
Professor Henry Krakauer, Physics
The College of William and Mary

Professor Shiwei Zhang, Physics
The College of William and Mary

Assistant Professor Enrico Rossi, Physics
The College of William and Mary

Associate Professor Seth Aubin, Physics
The College of William and Mary

Professor Andreas Stathopoulos, Computer Science
The College of William and Mary

ABSTRACT

Graphene, a single layer of hexagonally bonded carbon atoms, is often hailed as a wonder material due to its remarkable intrinsic properties. It is the thinnest, the strongest, and the most stretchable crystal ever measured. Of all semiconductors, it also exhibits the highest electron mobility and current density at room temperature. One potential application of graphene is for use in spintronic devices. However, external methods are required to induce magnetism on graphene, since pristine graphene is nonmagnetic. One proposal is to adsorb transition metal atoms to provide localized magnetic moments in graphene. Single Co atoms on graphene, in particular, have been extensively studied both theoretically and experimentally. Previous calculations, however, show significantly varying results on the bonding nature of Co/graphene system and none of the calculations is fully consistent with the experimental results. We investigate the stability and electronic properties of single Co atoms on graphene with near-exact auxiliary-field quantum Monte Carlo. Our findings are consistent with and provide an explanation for experimental results with Co on free-standing graphene.

TABLE OF CONTENTS

ACKNOWLEDGMENTS

First of all, I would like to thank my advisors, Professor Henry Krakauer and Professor Shiwei Zhang, for their support and guidance throughout my Ph.D. career. I also would like to thank Dr. Wirawan Purwanto for his important assistance in my research project. This dissertation would not have been possible without their support.

I would like to express my sincere gratitude to the Ph.D. defense committee members for their careful examination, correction, and feedback of my thesis. I would also like to thank the physics department administrative staff, Paula Perry, Elle Wilkinson, Carol Hankins, and Sylvia Stout, for their excellent support.

I am grateful for the fruitful discussions and friendship from my fellow research group members: Eric Walter, Enrico Rossi, Fengjie Ma, Driss Badiane, Simone Chiesa, Mingpu Qin, Junhua Zhang, Dan Pechkis, Jie Xu, Christopher Hendriks, Christopher Triola, Martin Rodriguez-Vega, Satrio Gani, Hao Shi, and Peter Rosenberg.

Finally I would like to thank my parents and sisters for their love and support for me.

I dedicate this dissertation to anyone who finds it useful.

LIST OF TABLES

LIST OF FIGURES

STABILITY, ENERGETICS, AND MAGNETIC STATES OF COBALT ADATOMS ON GRAPHENE: AN *AB INITIO* QUANTUM MONTE CARLO STUDY

CHAPTER 1

Introduction

Graphene is a monolayer sheet of carbon atoms densely packed in a honeycomb lattice. It has been studied theoretically for over sixty years [1], and is widely used for describing properties of various carbon-based materials. Although the fact that graphite, three-dimensional stacks of graphene layers, has been widely recognized since 1564 (the invention of the pencil), the isolation of individual graphene layers was presumed to be impossible. It was argued that strictly two-dimensional materials were unstable and could not exist due to thermal fluctuations [2]. However, in 2004, a research group at the University of Manchester succeeded in isolating and studying single graphene layers [3], and this groundbreaking work was awarded Nobel Prize in Physics for 2010.

Since its discovery, graphene has been the subject of intense research efforts to adapt it for a variety of promising applications due to its unique and exceptional intrinsic properties [2, 4, 5]. Structurally, graphene is the strongest, the stiffest, and the most stretchable crystal ever created [6]. Electronically, due to the linear dispersion of energy bands near the Dirac point, it has the highest electron mobility

and current density at room temperature of all semiconductors [7–9]. New and important findings continue to appear, making graphene research among the most dynamically evolving research areas.

One potential application of graphene is for use in spintronic devices [10–13]. Spintronic technology exploits both electron charge and spin to store and manipulate information. This new generation of technology will operate remarkably more efficient and faster than the current technology does [14, 15]. However, pristine graphene is nonmagnetic. Several approaches have been considered, for example, by introducing structural defects in graphene [16, 17] or creating edge orientation with graphene nanoribbons [18]. Another proposal is to adsorb transition metal atoms to provide localized magnetic moments in graphene.

Recently, single Co atoms on graphene have been extensively studied, both theoretically [19–34] and experimentally [35–42]. For example, scanning tunneling microscopy (STM) experiments have demonstrated the ability to controllably ionize a Co adatom on graphene using a back gate voltage [35]. A large magnetic anisotropy in Co/graphene systems has been observed [39, 42]. The observation of the Kondo effect caused by Co adatoms on graphene has been reported [41, 42]. The study of Co/graphene is thus of great interest both from a fundamental and applied perspective.

Previous theoretical studies have been focused on three high-symmetry Co adsorption sites, as shown in Fig. 5.1, i.e., the hollow, bridge, and top sites which describe a Co atom right above the center of the hexagonal ring, the middle of a C–C bond, and a carbon atom, respectively. These studies have addressed Co adsorption on graphene at the density functional theory (DFT) level, using local or semi-local functionals, or an empirical Hubbard on-site repulsion U (DFT+U) [19–31]. Although the approaches based on independent-electron approximations

have often given reasonable results in a variety of materials, the accuracy of these methods in the system of interest, combining a transition metal and graphene, is unclear since electron correlation effects can be significant. Indeed, widely varying results have been reported for the nature of the magnetic state, adsorption site, and binding energy of Co as a function of adsorption height.

For example, DFT calculations with the generalized gradient approximation (GGA) [43] predict [19–31] the sixfold hollow site is the global minimum, with an equilibrium height of $h_{\mathrm{eq}} \sim 1.5$ Å and a low-spin $3d^9 4s^0$ Co atom configuration ($S = 1/2$). A different functional, the hybrid Becke three-parameter Lee-Yang-Parr (B3LYP) [44], predicts [24] an equilibrium height of $h_{\mathrm{eq}} \sim 1.9$ Å at the hollow site, with a high-spin $3d^8 4s^1$ configuration ($S = 3/2$). Results from the GGA+U [45, 46] approach have shown sensitivity to the value of the parameter U used. For $U = 2$ eV, it predicts the global minimum to be the hollow site with a low-spin configuration, while for $U = 4$ eV, the global minimum is the top site with a high-spin configuration [23, 27, 31]. A perturbative quantum chemistry calculation based on a complete active space self-consistent field (CASSCF) [47] reference predicts the global minimum at the van der Waals (vdW) region with $h_{\mathrm{eq}} \sim 3.1$ Å and a high-spin $3d^7 4s^2$ configuration [32]. These varying results strongly indicate the need for better understanding of and fundamentally more accurate *ab initio* approaches to treat Co adsorption on graphene.

In this dissertation, we address the issue of the bonding nature of Co on graphene from two complementary angles, using the auxiliary-field quantum Monte Carlo (AFQMC) [48–50] method. First we apply an exact free-projection AFQMC approach to systematically benchmark the various theoretical methods in a series of model systems which are smaller in size but retain key features of Co/graphene. These results will provide guidance for future studies of transition metal adsorption

on graphene, especially in the selection of computationally less costly approaches. Second, a frozen-orbital embedding scheme is implemented to extend the system size that can be treated directly with AFQMC. Using the new approach, we determine the relative stability of different adsorption sites and magnetic states for Co/graphene by direct AFQMC calculations of Co on large substrates, augmented by a finite-size correction obtained with DFT. Our results are consistent with and provide a quantitative explanation for the observations from recent STM experiments of Co adatoms adsorbed on H-intercalated graphene/SiC(0001) [38].

The rest of this dissertation is organized as follows.

Chapter 2 provides a general overview of the many-body problem and several approximations to solve it. For independent-electron approximations, we will describe the mathematical formalism behind the Hartree-Fock (HF) and density functional theory (DFT) methods. Various correlated methods such as configuration interaction (CI), coupled cluster (CC), and quantum Monte Carlo (QMC) will also be discussed.

In Chapter 3, we review the auxiliary-field quantum Monte Carlo (AFQMC) method which provides most of the many-body results in this dissertation. We also discuss the phaseless approximation which controls the sign/phase problem in AFQMC.

In Chapter 4, we discuss two recent developments implemented in AFQMC, i.e., the frozen-orbital approximation and modified Cholesky decomposition. These improvements allow AFQMC to treat larger systems directly and efficiently without sacrificing its accuracy.

In Chapter 5, we present our principal results. Systematic AFQMC benchmark studies of various theoretical methods for three model systems: Co/C_6H_6, Co/C_2H_4, and Co/C_4H_8 are presented. These model systems represent prototypes of the three

high-symmetry Co adsorption sites. Equipped with the benchmark studies, we next examine the stability and magnetic properties of Co/graphene using frozen-orbital phaseless AFQMC. Finally we compare our results with the experimental observations. Our findings are in a good agreement with and provide a quantitative explanation for the observations from recent STM experiments of Co adatoms adsorbed on H-intercalated graphene/SiC(0001).

Chapter 6 summarizes our results and comments on the future prospects of Co/graphene research.

CHAPTER 2

Electronic Structure Methods

In principle, the behavior of ordinary matter can be fully described by the many-body Schrödinger equation. However, in most cases, the many-body problem can be extremely complex, and it is impossible to obtain the exact solution. Many approximations have been formulated, and they vary greatly in accuracy and computational cost. This chapter provides a general overview of mean-field and correlated methods to address the many-body problem.

2.1 Many-body Schrödinger Equation

The time-independent many-body Schrödinger equation can be written as

$$\hat{H}|\Psi\rangle = E|\Psi\rangle\,, \tag{2.1}$$

where $\hat{H}$ is the Hamiltonian operator of a system of nuclei and electrons. The Hamiltonian for N electrons and N_a nuclei is given by [51, 52]

$$\begin{aligned}\hat{H} &= \hat{T}_e + \hat{T}_n + \hat{U}_{ee} + \hat{U}_{nn} + \hat{U}_{en} \\ &= -\frac{\hbar^2}{2m_e}\sum_{i=1}^{N}\nabla_i^2 - \frac{\hbar^2}{2}\sum_{\alpha=1}^{N_a}\frac{\nabla_\alpha^2}{M_\alpha} + \frac{1}{2}\sum_{i=1}^{N}\sum_{j\neq i}^{N}\frac{e^2}{|\mathbf{r}_i - \mathbf{r}_j|} \\ &\quad + \frac{1}{2}\sum_{\alpha=1}^{N_a}\sum_{\beta\neq\alpha}^{N_a}\frac{Z_\alpha Z_\beta e^2}{|\mathbf{R}_\alpha - \mathbf{R}_\beta|} - \sum_{i=1}^{N}\sum_{\alpha=1}^{N_a}\frac{Z_\alpha e^2}{|\mathbf{r}_i - \mathbf{R}_\alpha|}\,,\end{aligned} \tag{2.2}$$

where m_e and $\mathbf{r}_i$ are the mass and the position of electron i, while M_α, Z_α, and $\mathbf{R}_\alpha$ are the mass, the atomic number, and the position of nucleus α, respectively. The Hamiltonian operator consists of kinetic energies of electrons, $\hat{T}_e$, and nuclei, $\hat{T}_n$, the repulsive Coulomb interactions between electrons, $\hat{U}_{ee}$, between nuclei, $\hat{U}_{nn}$, and the attractive Coulomb interactions between electrons and nuclei, $\hat{U}_{en}$.

Solving this equation is extremely difficult and the only known exact solution is for a hydrogen atom containing one electron and one proton. Therefore, it is necessary to make some approximations. Since the electronic mass is much smaller than the masses of atomic nuclei, $m_e << M_\alpha$, the electrons respond quickly to the much slower ionic motions. Therefore, electrons can be considered to be in their instantaneous ground state as the nuclei move. This is the well-known Born-Oppenheimer approximation [51, 52]. This approximation simplifies the electronic Hamiltonian into:

$$\hat{H} = -\frac{\hbar^2}{2m_e}\sum_{i=1}^{N}\nabla_i^2 + \frac{1}{2}\sum_{i=1}^{N}\sum_{j\neq i}^{N}\frac{e^2}{|\mathbf{r}_i - \mathbf{r}_j|} - \sum_{i=1}^{N}\sum_{\alpha=1}^{N_a}\frac{Z_\alpha e^2}{|\mathbf{r}_i - \mathbf{R}_\alpha|} + \hat{U}_{nn}\,. \tag{2.3}$$

Within this approximation, the kinetic energy of the nuclei can be neglected and the Coulomb interactions between the nuclei add a constant to the total energy of

the system.

2.2 Mean-field Methods

Mean-field approximations replace the two-body electron-electron interactions with an effective one-body potential.This effective potential encapsulates the many-body nature of the true system in an approximate way. This section will introduce two widely-used mean-field approximations, Hartree-Fock and density functional theory.

2.2.1 Hartree-Fock Approximation

The Hartree-Fock (HF) approximation [51, 52] assumes that the many-body wave function for a fixed number N of electrons is a single determinant, known as a Slater determinant. The HF wave function for N electrons with positions $\mathbf{r}_i$ and spin σ_i is given by

$$\Psi = \frac{1}{\sqrt{N!}} \begin{vmatrix} \phi_1(\mathbf{r}_1, \sigma_1) & \phi_1(\mathbf{r}_2, \sigma_2) & \dots & \phi_1(\mathbf{r}_N, \sigma_N) \\ \phi_2(\mathbf{r}_1, \sigma_1) & \phi_2(\mathbf{r}_2, \sigma_2) & \dots & \phi_2(\mathbf{r}_N, \sigma_N) \\ \vdots & \vdots & & \vdots \\ \phi_N(\mathbf{r}_1, \sigma_1) & \phi_N(\mathbf{r}_2, \sigma_2) & \dots & \phi_N(\mathbf{r}_N, \sigma_N) \end{vmatrix}, \tag{2.4}$$

where ϕ_i is a single particle wave function given by the product of a function of the position $\varphi_i(\mathbf{r}_j)$ and a function of the spin $\alpha_i(\sigma_j)$. This wave function automatically satisfies the Pauli exclusion principle since interchanging the position of two electrons is equivalent to interchanging the corresponding columns in the determinant, which changes its sign.

The total energy of the system with respect to the Hartree-Fock wave function

is given by

$$
\begin{aligned}
E &= \langle \Psi | H | \Psi \rangle \\
&= \sum_i \int \varphi_i^*(\mathbf{r}) \left(-\frac{\hbar^2}{2m_e} \nabla^2 + V_{\text{ion}}(\mathbf{r}) \right) \varphi_i(\mathbf{r}) d\mathbf{r} \\
&\quad + \frac{1}{2} \sum_{i,j(i \neq j)} \int \frac{e^2}{|\mathbf{r} - \mathbf{r}'|} |\varphi_i(\mathbf{r})|^2 |\varphi_j(\mathbf{r}')|^2 d\mathbf{r} d\mathbf{r}' \\
&\quad - \frac{1}{2} \sum_{i,j(i \neq j)} \int \varphi_i^*(\mathbf{r}) \varphi_j^*(\mathbf{r}') \frac{e^2}{|\mathbf{r} - \mathbf{r}'|} \delta_{\sigma_i \sigma_j} \varphi_i(\mathbf{r}) \varphi_j(\mathbf{r}') d\mathbf{r} d\mathbf{r}' + U_{nn} \,.
\end{aligned}
\tag{2.5}
$$

This equation has utilized the orthogonal property of the spin function $\alpha_i(\sigma_j)$. The first term contains only the one-body expectation values. The second and third terms, which arise from the electron-electron interaction, are known as the Hartree energy and the exchange energy.

The HF approach is to minimize the total energy with respect to φ_i which leads to the single-particle HF equations

$$
\left[-\frac{\hbar^2}{2m_e} \nabla^2 + V_{\text{ion}}(\mathbf{r}) + V_H(\mathbf{r}) \right] \varphi_i(\mathbf{r}) + \int v_x(\mathbf{r}, \mathbf{r}') \varphi_i(\mathbf{r}') d\mathbf{r}' = \epsilon_i \varphi_i(\mathbf{r}) \,, \tag{2.6}
$$

where $V_{\text{ion}}(\mathbf{r})$, $V_H(\mathbf{r})$, and $v_x(\mathbf{r}, \mathbf{r}')$ are ionic, Hartree and non-local exchange potentials, respectively, which can be written as

$$
V_{\text{ion}}(\mathbf{r}) = -\sum_{\alpha=1}^{N_a} \frac{Z_\alpha e^2}{|\mathbf{r} - \mathbf{R}_\alpha|} \,, \tag{2.7}
$$

$$
V_H(\mathbf{r}) = -\sum_j \int \frac{e^2}{|\mathbf{r} - \mathbf{r}'|} |\varphi_j(\mathbf{r}')|^2 d\mathbf{r}' \,, \tag{2.8}
$$

$$
v_x(\mathbf{r}, \mathbf{r}') = -\sum_j \frac{e^2}{|\mathbf{r} - \mathbf{r}'|} \varphi_j^*(\mathbf{r}') \varphi_j(\mathbf{r}) \delta_{\sigma_i \sigma_j} \,. \tag{2.9}
$$

Eq. (2.6) can be solved self-consistently. First we make a guess for a set of $\varphi_i(\mathbf{r})$'s to

construct the single-particle Hamiltonian, which allow us to solve the HF equations for each new $\varphi_i(\mathbf{r})$. This process is repeated iteratively until self-consistency is achieved. The final process will produce a set of orthonormal HF orbitals $\{\phi_i\}$ with eigenenergies $\{\epsilon_i\}$.

2.2.2 Density Functional Theory

In 1964 and 1965, Hohenberg, Kohn and Sham developed a different way of looking at the many-body problem, which has been called density functional theory (DFT) [53, 54]. They showed that all properties of the many-body system can be considered as unique functionals of the ground state of the total density of electrons $n(\mathbf{r})$. With this approach, the many-body wave function is not required to be explicitly specified, as was done in the HF approximations. DFT has been widely used to calculate the properties of molecules and solids, and its applications to different problems continue to grow.

We briefly reproduce the proof that the density $n(\mathbf{r})$ is a unique quantity for a given external potential (e.g., $V_{\text{ion}}(\mathbf{r})$) for the electrons. Assume that two different potentials $V(\mathbf{r})$ and $V'(\mathbf{r})$ give rise to the same density $n(\mathbf{r})$. The two potentials are different in a non-trivial way, meaning that they do not differ merely by a constant. We can define the total energy of the systems with Hamiltonians H and H', respectively, where the first hamiltonian contains $V(\mathbf{r})$ and the second $V'(\mathbf{r})$ as external potential:

$$E = \langle \Psi | H | \Psi \rangle \,, \tag{2.10}$$

$$E' = \langle \Psi' | H' | \Psi' \rangle \,. \tag{2.11}$$

From the variational principle, we obtain

$$\begin{aligned} E < \langle \Psi' | H | \Psi' \rangle &= \langle \Psi' | H + V' - V' | \Psi' \rangle = \langle \Psi' | H' + V - V' | \Psi' \rangle \\ &= \langle \Psi' | H' | \Psi' \rangle + \langle \Psi' | V - V' | \Psi' \rangle \\ &= E' + \langle \Psi' | V - V' | \Psi' \rangle \,. \end{aligned} \tag{2.12}$$

The strict inequality is necessary since the two potentials are different in non-trivial ways. By the same token, we can prove

$$E' < E - \langle \Psi | V - V' | \Psi \rangle \,. \tag{2.13}$$

By adding Eqs. (2.12) and (2.13), we get

$$E + E' < E + E' + \langle \Psi' | V - V' | \Psi' \rangle - \langle \Psi | V - V' | \Psi \rangle \,. \tag{2.14}$$

Since the density is $n(\mathbf{r}) = N \int |\Psi(\mathbf{r}, \mathbf{r}_2, ..., \mathbf{r}_N)|^2 d\mathbf{r}_2 ... d\mathbf{r}_N$, the last two terms on the right-hand side of Eq. (2.14) become

$$\int n'(\mathbf{r})[V(\mathbf{r}) - V'(\mathbf{r})]d\mathbf{r} - \int n(\mathbf{r})[V(\mathbf{r}) - V'(\mathbf{r})]d\mathbf{r} = 0 \,. \tag{2.15}$$

This means that $E + E' < E' + E$, which is incorrect. Therefore the densities cannot be the same. This shows that there is a one-to-one correspondence between an external potential $V(\mathbf{r})$ and the density $n(\mathbf{r})$.

This problem can be reduced to a set of non-interacting particles with the same density as the real system, by expressing the density in terms of wavefunctions, as

$$n(\mathbf{r}) = \sum_{i=1}^{N} |\varphi_i(\mathbf{r})|^2 \,. \tag{2.16}$$

The energy functional can then be written as

$$E[n(\mathbf{r})] = -\frac{\hbar^2}{2m_e}\sum_{i=1}^{N}\int \varphi_i^*(\mathbf{r})\nabla^2\varphi_i(\mathbf{r})d\mathbf{r} + \int n(\mathbf{r})V_{\text{ion}}(\mathbf{r})d\mathbf{r} + \frac{e^2}{2}\int \frac{n(\mathbf{r})n(\mathbf{r}')}{|\mathbf{r}-\mathbf{r}'|}d\mathbf{r}d\mathbf{r}' + E_{xc}[n(\mathbf{r})]\,. \tag{2.17}$$

In this expression, the first term on the right-hand side is the kinetic energy of the system. The second and the third terms are the interaction energy with the ionic potential and the Coulomb interaction between electrons. The last term is called exchange-correlation energy which contains all the effects of the many-body character of the true system.

Minimizing Eq. (2.17) with respect to the wave function $\varphi_i(\mathbf{r})$, we obtain the Kohn-Sham equation

$$\left(-\frac{\hbar^2}{2m_e}\nabla^2 + V_{eff}(\mathbf{r}, n(\mathbf{r}))\right)\varphi_i(\mathbf{r}) = \epsilon_i\varphi_i(\mathbf{r})\,, \tag{2.18}$$

where the effective local potential is given by

$$V_{eff}(\mathbf{r}, n(\mathbf{r})) = V_{\text{ion}}(\mathbf{r}) + e^2\int \frac{n(\mathbf{r}')}{|\mathbf{r}-\mathbf{r}'|}d\mathbf{r}' + \frac{\delta E_{xc}[n(\mathbf{r})]}{\delta n(\mathbf{r})}\,. \tag{2.19}$$

This equation can be solved iteratively until self-consistency is reached. Unfortunately, the exact exchange-correlation functional is unknown and has to be approximated in some way.

The most well-known approximation for $E_{xc}[n(\mathbf{r})]$ is the local-density approximation (LDA):

$$E_{xc}^{\text{LDA}}[n(\mathbf{r})] = \int n(\mathbf{r})\varepsilon_{xc}[n(\mathbf{r})]d\mathbf{r}\,, \tag{2.20}$$

where $\varepsilon_{xc}[n(\mathbf{r})]$ is the exchange-correlation energy per particle of a homogeneous electron gas with charge density $n(\mathbf{r})$ calculated from quantum Monte Carlo simulation [55, 56]. There are many other approximations to E_{xc}, such as generalized gradient approximations or hybrid functionals. The search for better functionals is an active research area [57]. Later we will benchmark some of the most common DFT functionals for our model systems.

2.3 Explicitly Correlated Methods

There are various correlated methods to solve many-body problem. This section will discuss two widely-used correlated methods, coupled cluster (CC) and quantum Monte Carlo (QMC). We will also include the configuration interaction (CI) method because it is conceptually the simplest, although still challenging computationally. The quantity of interest, which correlated methods try to produce, is the correlation energy (E_{corr}) which is defined as the difference between the energy in the Hartree-Fock limit (E_{HF}) and the exact energy of a system (E_{exact})

$$E_{\text{corr}} = E_{\text{exact}} - E_{HF}\,. \tag{2.21}$$

The correlation energy is always negative by definition, because the Hartree-Fock energy is an upper bound to the exact energy.

2.3.1 Configuration Interaction

The HF approach can be improved by using a wave function with multiple determinants instead of single determinant. This multideterminant wave function is constructed from a set of determinants which includes the ground state determinant

$|\Psi_0\rangle$, the singly excited determinants $|\Psi_S\rangle$, the doubly excited determinants $|\Psi_D\rangle$, and so on up to N-tuply excited determinants. This approach is called configuration interaction (CI) [58, 59] and the many-body wave function $|\Phi_0\rangle$ can be written as

$$|\Phi\rangle = c_0|\Psi_0\rangle + \sum_{\mathrm{S}} c_{\mathrm{S}}|\Psi_{\mathrm{S}}\rangle + \sum_{\mathrm{D}} c_{\mathrm{D}}|\Psi_{\mathrm{D}}\rangle + \sum_{\mathrm{T}} c_{\mathrm{T}}|\Psi_{\mathrm{T}}\rangle + \sum_{\mathrm{Q}} c_{\mathrm{Q}}|\Psi_{\mathrm{Q}}\rangle + \dots , \quad (2.22)$$

where the subscripts S, D, T, and Q refer to single, double, triple, and quadrupole excitations, respectively. The total energy is minimized under the constraint that the total CI wave function is normalized. The ground-state and all the excited-state configurations are orthogonal to each other. This approach is exact in the limit that the basis set approaches completeness, which is called full CI (FCI).

The computational cost of FCI scales exponentially with the number of electrons, making it feasible only for small systems and modest basis sets. Therefore, in practice, we need to truncate the number of determinants included in the construction of the wave function. For example, we can consider only some of the excitation terms in Eq. (2.22). This results in the CIS (CI with single excitations), CISD (CI with single and double excitations), CISDT (CISD with triple excitations), and CISDTQ (CISD plus triple and quadrupole excitations). Taking into account higher order excitations is very rare due to the computational cost.

A CI calculation where both the coefficients in front of the determinants and the orbitals used for constructing the determinants are optimized is called a multiconfigurational self-consistent field (MCSCF) method. The MCSCF optimization is done iteratively until it reaches self-consistency. The major problem with MCSCF methods is selecting proper configurations to be included in the calculation. One widely used option is the complete active space self-consistent field (CASSCF) method. In this method, the molecular orbitals are divided into inactive orbitals,

which are always doubly occupied or empty, and active orbitals. The active orbitals will typically consist of some of the highest occupied and some of the lowest unoccupied orbitals obtained from a HF calculation. A more detailed discussion can be found in Ref. 59.

2.3.2 Coupled Cluster

Coupled cluster (CC) theory is widely recognized by the quantum chemistry community as being one of the most powerful and most accurate theories of the quantum many-electron problem [60–62]. It constructs a multi-electron wave function from a reference wave function, which is typically a Slater determinant obtained from Hartree-Fock molecular orbitals, using the exponential cluster operator to account for electron correlation. The CC wave function is written as an exponential ansatz:

$$|\Phi_{\mathrm{CC}}\rangle = e^{\hat{T}}|\Phi_0\rangle = (1 + \hat{T} + \frac{\hat{T}^2}{2!} + \frac{\hat{T}^3}{3!} + \dots)|\Phi_0\rangle\,, \tag{2.23}$$

with the cluster operator **T** is given by

$$\hat{T} = \hat{T}_1 + \hat{T}_2 + \hat{T}_3 + \cdots + \hat{T}_{N_{\mathrm{elec}}}\,, \tag{2.24}$$

and

$$\hat{T}_n = (n!)^{-2} \sum_{i,j,k,\dots}^{N_{\mathrm{o}}} \sum_{a,b,c,\dots}^{N_{\mathrm{v}}} t_{ijk\dots}^{abc\cdots} \hat{c}_a^\dagger \hat{c}_b^\dagger \hat{c}_c^\dagger \dots \hat{c}_k \hat{c}_j \hat{c}_i\,, \tag{2.25}$$

where the coefficient t's are called cluster amplitudes. Here $i, j, k, \dots$ label occupied HF states and $a, b, c, \dots$ label unoccupied states. The $\hat{T}_i$ operator, acting on a HF

reference wave function $|\Phi_0\rangle$, will generate all the ith excited Slater determinants:

$$\begin{aligned}
\hat{T}_1|\Phi_0\rangle &= \sum_{i}^{N_\mathrm{o}} \sum_{a}^{N_\mathrm{v}} t_i^a |\Phi_i^a\rangle \,, \\
\hat{T}_2|\Phi_0\rangle &= \sum_{i<j}^{N_\mathrm{o}} \sum_{a<b}^{N_\mathrm{v}} t_{ij}^{ab} |\Phi_{ij}^{ab}\rangle \,, \\
\hat{T}_3|\Phi_0\rangle &= \sum_{i<j<k}^{N_\mathrm{o}} \sum_{a<b<c}^{N_\mathrm{v}} t_{ijk}^{abc} |\Phi_{ijk}^{abc}\rangle \,, \\
&\ldots \,.
\end{aligned} \tag{2.26}$$

Applying the Hamiltonian operator to the CC wave function, we can obtain

$$\hat{H} e^{\hat{T}} |\Phi_0\rangle = E e^{\hat{T}} |\Phi_0\rangle \,. \tag{2.27}$$

To obtain an expression for the energy, we can left-multiply this equation by the reference wave function

$$\langle \Phi_0 | \hat{H} e^{\hat{T}} |\Phi_0\rangle = E \langle \Phi_0 | e^{\hat{T}} |\Phi_0\rangle = E \,, \tag{2.28}$$

where intermediate normalization, $\langle \Phi_0 | \Phi_\mathrm{CC} \rangle = 1$, is assumed. The expressions for cluster amplitudes can be obtained by left-projecting the Schrödinger equation with the excited Slater determinants

$$\langle \Phi_{ijk\ldots}^{abc\ldots} | \hat{H} e^{\hat{T}} |\Phi_0\rangle = E \langle \Phi_{ijk\ldots}^{abc\ldots} | e^{\hat{T}} |\Phi_0\rangle \,. \tag{2.29}$$

Although Eqs. 2.28 and 2.29 are useful to understand the formalism of the coupled cluster theory, the computer implementation for these equations are not manageable. A more practical approach is obtained by first multiplying Eq. 2.27 with the

inverse of the exponential operator $e^{-\hat{T}}$. The modified energy and cluster amplitude equations are given by

$$\langle \Phi_0 | e^{-\hat{T}} \hat{H} e^{\hat{T}} | \Phi_0 \rangle = E \,, \tag{2.30}$$

and

$$\langle \Phi_{ijk\ldots}^{abc\ldots} | e^{-\hat{T}} \hat{H} e^{\hat{T}} | \Phi_0 \rangle = 0 \,. \tag{2.31}$$

Eqs. 2.30 and 2.31 are equivalent to Eqs. 2.28 and 2.29 (see Refs. 60 and 61 for more detailed discussion).

The key point of CC theory is that the truncation of $\hat{T}$ is in the exponent. This leads to a finite number of terms on the left-hand side of Eqs. 2.30 and 2.31, as discussed in Refs. 60 and 61. Including only the first excitation, $\hat{T}_1$, will not improve the HF energy since the matrix elements between the HF and singly excited states are zero. Therefore the lowest excitation level is $\hat{T} = \hat{T}_2$, dubbed as coupled cluster doubles (CCD). A more complete model is given by CCSD which includes both single and double excitations, $\hat{T} = \hat{T}_1 + \hat{T}_2$. Both CCD and CCSD scale as M^6 where M is the size of the basis set used. The next higher level includes also the triple excitation, $\hat{T} = \hat{T}_1 + \hat{T}_2 + \hat{T}_3$, called CCSDT which scales as M^8. It is common to assume that CCSDTQ is approximately exact; due to its computational cost, it can only be used for small systems. The most widely-used CC method is CCSD(T) which includes triple excitations as a perturbative correction and scales as M^7.

2.3.3 Quantum Monte Carlo

Quantum Monte Carlo (QMC) methods represent a powerful and accurate computational technique for solving the many-body Schrödinger equation in a broad range of physical systems [63, 64]. The algorithms are highly parallel, allowing it to take full advantage of high-performance computing systems. The computational scaling of most QMC methods is also favorable, M^3 or M^4, compared to CCSD(T)'s which is M^7.

The most basic and simplest QMC method is variational Monte Carlo (VMC). In the VMC method, the true ground state $|\Psi_0\rangle$ is approximated by a trial wave function $|\Psi_{\mathrm{T}}\rangle$. $|\Psi_{\mathrm{T}}\rangle$ may be predefined and may also depend on a set of parameters which are optimized to minimize the energy expectation value

$$E_{\Psi_{\mathrm{T}}} = \frac{\int \Psi_{\mathrm{T}}^*(\mathbf{R})\hat{H}\Psi_{\mathrm{T}}(\mathbf{R})d\mathbf{R}}{\int \Psi_{\mathrm{T}}^*(\mathbf{R})\Psi_{\mathrm{T}}(\mathbf{R})d\mathbf{R}}\,, \tag{2.32}$$

where $\mathbf{R} = (\mathbf{r}_1, \mathbf{r}_2, \ldots, \mathbf{r}_N)$ is a $3N$-dimensional vector describing the coordinates of all N particles in the system.

The variational principle states that this is an upper bound to the true ground state energy. This highly-dimensional integral is difficult to solve. The VMC method evaluates this integral stochastically and treats the non-separable wave functions directly. The VMC energy can be written as

$$E_{\mathrm{VMC}} = \frac{\int |\Psi_{\mathrm{T}}(\mathbf{R})|^2[\Psi_{\mathrm{T}}^{-1}(\mathbf{R})\hat{H}\Psi_{\mathrm{T}}(\mathbf{R})]d\mathbf{R}}{\int |\Psi_{\mathrm{T}}(\mathbf{R})|^2 d\mathbf{R}}\,. \tag{2.33}$$

The Metropolis algorithm is used to sample a set of point $\{\mathbf{R}_i : i = 1 \ldots \mathcal{N}\}$ from the configuration-space probability density $\mathcal{P}(\mathbf{R}) = |\Psi_{\mathrm{T}}(\mathbf{R})|^2 / \int |\Psi_{\mathrm{T}}(\mathbf{R})|^2 d\mathbf{R}$. The quantity $E_{\mathrm{L}}(\mathbf{R}) = \Psi_{\mathrm{T}}^{-1}(\mathbf{R})\hat{H}\Psi_{\mathrm{T}}(\mathbf{R})$, referred as the local energy, is evaluated at

each of these points and the average energy accumulated is given by

$$E_{\mathrm{VMC}} = \frac{1}{\mathcal{N}} \sum_{i}^{\mathcal{N}} E_{\mathrm{L}}(\mathbf{R}_i)\,. \tag{2.34}$$

The variational energy E_{VMC} is a stochastic variable and its error scales as $\mathcal{N}^{-1/2}$.

The accuracy of the VMC method is limited by the quality of $|\Psi_{\mathrm{T}}\rangle$. This limitation can be resolved by ground state projection methods. Unlike the many-body wave function based methods above, projection QMC methods use the wave function only implicitly, sampling it to calculate expectation values. These QMC methods obtain the ground-state wave function $|\Psi_0\rangle$ by applying the imaginary time projection operator to a chosen reference on trial wave function $|\Psi_{\mathrm{T}}\rangle$

$$|\Psi_0\rangle \propto \lim_{\tau\to\infty} e^{-\tau\hat{H}}|\Psi_{\mathrm{T}}\rangle\,. \tag{2.35}$$

The $|\Psi_{\mathrm{T}}\rangle$ can be any known trial state as long as it satisfies $\langle\Psi_{\mathrm{T}}|\Psi_0\rangle \neq 0$. The difference between different classes of QMC methods is in the way they carry out this projection.

The diffusion Monte Carlo (DMC) represents $|\Psi_{\mathrm{T}}\rangle$ in real space. DMC simulations for fermionic systems suffer from the sign problem [48], which arises from the antisymmetric nature of fermion wave function. The fixed-node approximation [65] is introduced to address this problem by imposing the nodes of a reference wavefunction. The fixed-node DMC energy is variational, i.e. it is the upper bound to the exact ground-state energy. The accuracy of this approximation is entirely dependent on the nodes of the reference wavefunction. For a more detailed review of DMC, see Refs. 63 and 66.

There are also other projector QMC methods such as Green's function QMC,

path-integral QMC, and auxiliary-field QMC. We will discuss AFQMC in more detail in Chapter 3.

CHAPTER 3

Auxiliary Field Quantum Monte Carlo

Auxiliary Field Quantum Monte Carlo (AFQMC) is one of the most accurate QMC methods and has been applied to study a wide variety of material systems [33, 34, 49, 67–79]. For system with moderate correlation, its accuracy has been shown to be similar to the CCSD(T) method, the gold-standard in quantum chemistry, near equilibrium geometries and better for bond-breaking [34, 69, 73, 76, 77]. AFQMC has also been shown to be accurate for strongly correlated systems [**?**]. It has a low algebraic scaling with the system size, $M^3 - M^4$ (M is the number of the one-particle basis functions), and its implementation on massively parallel supercomputers is straightforward.

The AFQMC method [48–50] evaluates stochastically the ground-state properties of a many-body Hamiltonian by means of random walks with Slater determinants expressed in a chosen single-particle basis. This sampling process in Slater determinant space automatically incorporates the antisymmetric nature of

the fermionic wave function. The stochastically generated determinants are the samples of the ground-state many-body wave function. Although AFQMC is an exact method in principle, the fermion sign problem causes an exponential growth of the Monte Carlo variance. The problem is controlled using the phaseless approximation [49], which imposes a constraint on the overall phase of the Slater determinants using a trial wave function $|\Psi_{\mathrm{T}}\rangle$.

In extensive benchmarks in both strongly correlated lattice models and molecular and crystalline systems, phaseless AFQMC has shown excellent agreement with exact and/or experimental results [49, 69–76]. In most calculations on realistic systems (molecules and solids), trial wave functions of a single Slater determinant from Hartree-Fock or DFT have been used and have been shown to give accurate results. The sign problem can also be attacked directly by lifting or releasing the phaseless constraint, using a large number of random walkers. This approach is exact, although exponetially scaling in computational cost with system size, and will be referred to as free-projection AFQMC (FP-AFQMC) [49, 77, 80].

The AFQMC method has been developed for two types of basis set: planewaves with pseudopotentials, which are suitable for studying periodic systems, and Gaussian type orbitals (GTO), which are widely employed for *ab initio* quantum chemistry calculations. In addition, AFQMC also has been applied to lattice models (e.g., the Hubbard model) which typically have correlation energy as a significantly higher fraction of their total energy than in most molecules and solids [81, 82]. In this dissertation, we use both the free-projection and phaseless AFQMC methods working with standard GTO basis sets (GTO-AFQMC) together with an implementation of the frozen-core approximation to treat the inner core electrons [83]. We also implemented a frozen-orbital approach to allow direct AFQMC calculations on large system sizes. We will discuss these recent developments in AFQMC in the

next chapter.

3.1 Ground State Projection

The general many-body Hamiltonian can be expressed in second-quantized representation as [84, 85]

$$\hat{H} = \hat{T} + \hat{V} = \sum_{i,j}^{M} T_{ij} c_i^\dagger c_j + \frac{1}{2} \sum_{i,j,k,l}^{M} V_{ijkl} c_i^\dagger c_j^\dagger c_k c_l \,, \tag{3.1}$$

where M is the size of the chosen one-particle basis, and $c_i^\dagger$ and c_i are the corresponding creation and annihilation operators. The one-body matrix elements, T_{ij}, contain the effect from both the kinetic energy and external potential, while the two-body matrix elements, V_{ijkl}, contain the effect of the electron-electron interaction. The matrix elements are given by integrals expressed in terms of the basis functions [69, 74].

The AFQMC method projects the ground-state wave function $|\Psi_0\rangle$ from a trial wave function $|\Psi_\mathrm{T}\rangle$, assuming $\langle\Psi_\mathrm{T}|\Psi_0\rangle \neq 0$,

$$|\Psi_0\rangle \propto \lim_{\tau\to\infty} e^{-\tau\hat{H}} |\Psi_\mathrm{T}\rangle \,. \tag{3.2}$$

Ground-state expectation value of a physical observable $\hat{O}$ is given by

$$\langle\hat{O}\rangle = \frac{\langle\Psi_0|\hat{O}|\Psi_0\rangle}{\langle\Psi_0|\Psi_0\rangle} \,. \tag{3.3}$$

If the operator $\hat{O}$ commutes with $\hat{H}$, a so-called mixed estimator can be used to calculate the expectation $\langle\hat{O}\rangle$ and provide significant simplifications in numerical calculation. With a mixed estimator, the ground-state energy E_0 can be obtained

from a trial wave function $|\Psi_{\mathrm{T}}\rangle$

$$E_0 = \frac{\langle \Psi_{\mathrm{T}}|\hat{H}|\Psi_0\rangle}{\langle \Psi_{\mathrm{T}}|\Psi_0\rangle} = \lim_{\tau\to\infty} \frac{\langle \Psi_{\mathrm{T}}|\hat{H}e^{-\tau\hat{H}}|\Psi_{\mathrm{T}}\rangle}{\langle \Psi_{\mathrm{T}}|e^{-\tau\hat{H}}|\Psi_{\mathrm{T}}\rangle}\,. \tag{3.4}$$

In practice, the limit is obtained iteratively by

$$e^{-\Delta\tau\hat{H}}e^{-\Delta\tau\hat{H}}\ldots e^{-\Delta\tau\hat{H}}|\Psi_{\mathrm{T}}\rangle \to |\Psi_0\rangle\,, \tag{3.5}$$

where $\Delta\tau$ is a small time step. The input $|\Psi_{\mathrm{T}}\rangle$ can be either a single Slater determinant or a multideterminant wave function. The AFQMC projection produces a stochastic multideterminant representation of the ground-state wave function $|\Psi_0\rangle$.

3.2 Hubbard-Stratonovich Transformation

In order to carry out the projection procedure in Slater-determinant space, we write the many-body propagator, $e^{-\Delta\tau\hat{H}}$, in single-particle form. For a small $\Delta\tau$, a short-time Trotter-Suzuki decomposition [86, 87] can be used

$$e^{-\Delta\tau\hat{H}} = e^{-\Delta\tau\hat{T}/2}e^{-\Delta\tau\hat{V}}e^{-\Delta\tau\hat{T}/2} + \mathcal{O}\left(\Delta\tau^3\right)\,, \tag{3.6}$$

where the last term on the right-hand side is known as Trotter error. The Trotter error can be reduced with an extrapolation procedure after separate calculations with different values of $\Delta\tau$ have been done.

The implementation of the one-body projector $e^{-\Delta\tau\hat{T}/2}$ is straightforward since the operator $e^{-\Delta\tau\hat{T}}$ acting on a Slater determinant gives another Slater determinant. In order to evaluate the two-body projector $e^{-\Delta\tau\hat{H}}$, we first decompose $\hat{H}$ into a sum

of squares of one-body operators

$$\hat{V} = -\frac{1}{2}\sum_{\gamma} \hat{v}_{\gamma}^{2} + (\text{one-body terms})\,, \tag{3.7}$$

where the minus sign is a notational convention. The additional one-body terms arise from reordering the creation and annihilation operators. Next we use the Hubbard-Stratonovich (HS) transformation [88, 89] to rewrite the two-body operator $e^{-\Delta\tau\hat{H}}$ as a multidimensional integral

$$e^{(1/2)\tau\sum_{\gamma}\hat{v}_{\gamma}^{2}} \underset{\tau\to 0}{=} \prod_{\gamma}\int_{-\infty}^{\infty}\frac{d\sigma_{\gamma}}{\sqrt{2\pi}}e^{-\sigma_{\gamma}^{2}/2}e^{\sqrt{\tau}\,\sigma_{\gamma}\hat{v}_{\gamma}}\,, \tag{3.8}$$

where $\{\sigma_{\gamma}\}$ are auxiliary-field variables. This integral is evaluated stochastically in AFQMC. In the limit of $\Delta\tau \to 0$, both Eqs. (3.6) and (3.8) are exact. Therefore we have an exact reformulation of the original ground-state projector in terms of one-body projection operators $\{\hat{v}_{\gamma}\}$ coupled with fictitious external auxiliary fields $\{\sigma_{\gamma}\}$ which recovers the original two-body interactions.

3.3 Importance Sampling and Phaseless Approximation

Summarizing, we can express the projection operator as a high-dimensional integral over auxiliary fields $\boldsymbol{\sigma}$,

$$e^{-\tau\hat{H}} = \int P(\boldsymbol{\sigma})B(\boldsymbol{\sigma})d\boldsymbol{\sigma}\,, \tag{3.9}$$

where $P(\boldsymbol{\sigma})$ is the normal distribution function, and

$$B(\boldsymbol{\sigma}) = e^{-\tau\hat{K}/2} e^{\sqrt{\tau}\,\boldsymbol{\sigma}\cdot\hat{\boldsymbol{v}}} e^{-\tau\hat{K}/2} \tag{3.10}$$

is a one-body propagator. With this representation, the operator in the integrand can simply act on a Slater determinant and yield another determinant

$$B(\boldsymbol{\sigma})|\phi\rangle \rightarrow |\phi'\rangle\,. \tag{3.11}$$

The ground-state energy can be calculated by stochastically sampling the mixed estimator in Eq. (3.4). The initial population of walkers is usually set equal to $|\Psi_{\mathrm{T}}\rangle$. In general, the one-body operators $\hat{\boldsymbol{v}}$ are complex. Therefore the orbitals in $|\phi\rangle$ will become complex and the statistical fluctuations in the mixed estimator grow exponentially with projection time. This phase problem is controlled with the phaseless approximation [49] based on the complex importance function $\langle\Psi_{\mathrm{T}}|\phi\rangle$. We modify Eq. (3.9) to obtain the following new propagator

$$\int \langle\Psi_{\mathrm{T}}|\phi'(\boldsymbol{\sigma}-\bar{\boldsymbol{\sigma}})\rangle P(\boldsymbol{\sigma}-\bar{\boldsymbol{\sigma}}) B(\boldsymbol{\sigma}-\bar{\boldsymbol{\sigma}}) \frac{1}{\langle\Psi_{\mathrm{T}}|\phi\rangle} d\boldsymbol{\sigma}\,, \tag{3.12}$$

where a constant shift $\bar{\sigma}$ has been included in the integral in Eq. (3.9). Equation (3.12) can be rewritten as

$$\int P(\boldsymbol{\sigma}) W(\boldsymbol{\sigma}, \bar{\boldsymbol{\sigma}}) B(\boldsymbol{\sigma}-\bar{\boldsymbol{\sigma}}) d\boldsymbol{\sigma}\,, \tag{3.13}$$

where

$$W(\boldsymbol{\sigma}, \bar{\boldsymbol{\sigma}}) \equiv \frac{\langle\Psi_{\mathrm{T}}|B(\boldsymbol{\sigma}-\bar{\boldsymbol{\sigma}})|\phi\rangle}{\langle\Psi_{\mathrm{T}}|\phi\rangle} e^{\boldsymbol{\sigma}\cdot\bar{\boldsymbol{\sigma}} - \bar{\boldsymbol{\sigma}}\cdot\bar{\boldsymbol{\sigma}}/2}\,, \tag{3.14}$$

The one-body operator $B(\boldsymbol{\sigma}-\bar{\boldsymbol{\sigma}})$ generates the random walker stream, transforming $|\phi\rangle$ into $|\phi'\rangle$, while $W(\boldsymbol{\sigma},\bar{\boldsymbol{\sigma}})$ updates the weight factor $w_{\phi'} = W(\boldsymbol{\sigma},\bar{\boldsymbol{\sigma}})w_\phi$.

The optimal choice of the "force bias" $\bar{\boldsymbol{\sigma}}$, which minimizes weight fluctuations to $\mathcal{O}(\sqrt{\tau})$, is given by

$$\bar{\boldsymbol{\sigma}} = -\sqrt{\tau}\frac{\langle\Psi_{\mathrm{T}}|\hat{\boldsymbol{v}}|\phi\rangle}{\langle\Psi_{\mathrm{T}}|\phi\rangle}\,. \tag{3.15}$$

With this choice, the weight W can be written as

$$W(\boldsymbol{\sigma},\bar{\boldsymbol{\sigma}}) \doteq exp\left[-\tau\frac{\langle\Psi_{\mathrm{T}}|\hat{H}|\phi\rangle}{\langle\Psi_{\mathrm{T}}|\phi\rangle}\right] \equiv e^{-\tau E_L[\phi]}\,, \tag{3.16}$$

where $E_L[\phi]$ is the local energy of each walker defined as

$$E_L[\phi] = \frac{\langle\Psi_{\mathrm{T}}|\hat{H}|\phi\rangle}{\langle\Psi_{\mathrm{T}}|\phi\rangle}\,. \tag{3.17}$$

With this approximation, the mixed estimator for the ground-state energy is phaseless and can be expressed as a weighted sum over the walkers

$$E_0 = \frac{\sum_\phi w_\phi E_L[\phi]}{\sum_\phi w_\phi}\,. \tag{3.18}$$

The weight w_ϕ is accumulated over the random walk.

There is still a problem however, as a finite density of walkers in the $\langle\Psi_{\mathrm{T}}|\phi\rangle$ complex plane can occur. To prevent this, a one-dimensional projection is implemented on the walkers. A phase rotation angle of the walker $|\phi\rangle$ is defined by

$$\Delta\theta \equiv \arg\left(\frac{\langle\Psi_{\mathrm{T}}|\phi'\rangle}{\langle\Psi_{\mathrm{T}}|\phi\rangle}\right) \tag{3.19}$$

and the walker weight is projected to its real, positive value [49],

$$w_{\phi'} \leftarrow \begin{cases} \cos(\Delta\theta)|W(\boldsymbol{\sigma}, \bar{\boldsymbol{\sigma}})|w_{\phi}, & |\Delta\theta| < \pi/2 \\ 0, & \text{otherwise} \end{cases} . \tag{3.20}$$

It is advantageous computationally to first subtract the mean-field background from the two-body potential in Eq. 3.7 before applying the HS transformation [68, 70, 77]

$$\frac{1}{2}\hat{v}^2 = \frac{1}{2}(\hat{\boldsymbol{v}} - \bar{\boldsymbol{v}}_{\mathrm{mf}})^2 + \hat{\boldsymbol{v}} \cdot \bar{\boldsymbol{v}}_{\mathrm{mf}} - \frac{1}{2}\bar{\boldsymbol{v}}_{\mathrm{mf}}^2 , \tag{3.21}$$

where $\bar{\boldsymbol{v}}_{\mathrm{mf}}$ is generally chosen to be the expectation value of the $\hat{\boldsymbol{v}}$ operator with respect to the trial wave function,

$$\bar{\boldsymbol{v}}_{\mathrm{mf}} \equiv \frac{\langle \Psi_{\mathrm{T}} | \hat{\boldsymbol{v}} | \Psi_{\mathrm{T}} \rangle}{\langle \Psi_{\mathrm{T}} | \Psi_{\mathrm{T}} \rangle} . \tag{3.22}$$

Although Eqs. 3.7 and 3.21 are equivalent, Eq. 3.21 leads to an improved $\Delta\tau$ extrapolation behavior [70]. Detailed discussions of the formalism can be found in Refs. 49, 68, 70 and 77.

CHAPTER 4

Recent Developments in AFQMC

Although the computational scaling of AFQMC is similar to that of DFT, the prefactor for AFQMC is significantly larger. Compared to DFT, this constrains the system size that can be treated with AFQMC. Furthermore, the Hamiltonian in Eq. 3.7, which is a preliminary setup step to the actual AFQMC calculations, has a memory bottleneck with a GTO basis if direct methods are used. The straightforward approach of simply diagonalizing V_{ijkl} in Eq. 3.1 is unfeasible for $M \gtrsim 300$. Here we describe methods that can be used to alleviate these problems. A frozen-orbital approximation [83] was recently implemented, which greatly reduces the relevant degrees of freedom and/or the number of explicitly correlated electrons in AFQMC calculations. We also implemented Cholesky decomposition [78] to remove a preprocessing bottleneck for computer time and memory, allowing the use of large GTO basis sets in AFQMC. These improvements allow AFQMC to treat directly larger systems more efficiently without sacrificing its accuracy.

4.1 Frozen-Orbital Approximation

It is often possible to partition the N-electron Hilbert space into active ($\mathbb{A}$) and inactive ($\mathbb{I}$) parts. The partitioning depends on physical considerations based on energetic, spatial, or other factors. Although the many-body wave function is never explicit in AFQMC, its random walkers are Slater determinants whose orbitals are expressed in terms of any one-particle orbital basis. Therefore there is a freedom to use any orthonormal basis in expressing the many-body wave function for partitioning the N-electron Hilbert space. The electrons in the inactive space are constrained to occupy the orbitals obtained by a lower-level theory, such as the canonical orbitals in HF, DFT, or natural orbitals determined from approximate CI calculation. The orthogonality constraint on the active space orbitals is implicitly imposed.

In order to implement this approach, little modification of the AFQMC formalism described in previous chapter is needed. An efficient approach is to define a frozen-orbital Hamiltonian $\hat{H}_{\mathbb{A}}$ that acts only on the $\mathbb{A}$ part of the Hilbert space. This approach will make the $\mathbb{I}$ orbitals appear explicitly only in one-body operators acting on the $\mathbb{A}$ space. We assume the separability of the many-body wave function:

$$\Psi \approx \mathcal{A}(\Psi_{\mathbb{I}}\Psi_{\mathbb{A}})\,, \tag{4.1}$$

where the wave functions $\Psi_{\mathbb{I}}$ and $\Psi_{\mathbb{A}}$ are assumed to be mutually orthogonal and individually antisymmetrized and normalized. The antisymmetrizer $\mathcal{A}$ permutes electrons between $\Psi_{\mathbb{I}}$ and $\Psi_{\mathbb{A}}$. This approach allows the total energy of the system

to be mapped onto an equivalent system involving only the $\mathbb{A}$ electrons:

$$E = \langle \Psi | \hat{H} | \Psi \rangle = \langle \Psi_{\mathbb{A}} | \hat{H}_{\mathbb{A}} | \Psi_{\mathbb{A}} \rangle \,, \tag{4.2}$$

where the frozen orbital Hamiltonian $\hat{H}_{\mathbb{A}}$ is given by

$$\begin{aligned} \hat{H}_{\mathbb{A}} = & \sum_{ij \in \mathbb{A}} K_{ij} c_i^\dagger c_j + \frac{1}{2} \sum_{ijkl \in \mathbb{A}} V_{ijkl} c_i^\dagger c_j^\dagger c_k c_l \\ & + \sum_{ij \in \mathbb{A}} V_{ij}^{\mathbb{I}\text{-}\mathbb{A}} c_i^\dagger c_j + E^{\mathbb{I}} \,. \end{aligned} \tag{4.3}$$

The first term includes the kinetic energy and all one-body external potentials acting on the $\mathbb{A}$ electrons. The second term is the Coulomb interactions among the $\mathbb{A}$ electrons. The third term includes one-body interactions between the $\mathbb{A}$ and $\mathbb{I}$ orbitals. The last term is a constant energy which represents all interactions among the $\mathbb{I}$ electrons. With the mapping defined in Eqs. (4.2) and (4.3), all of the AFQMC formalism described in previous chapter can be immediately used. Further details can be found in Ref. 83.

4.1.1 Frozen-Core Approximation

The Frozen-core (FC) approximation is one of the most broadly used example of the idea of partitioning the Hilbert space into active and inactive subspaces. With this approximation, the many-body wave function is expanded as sums of Slater determinants with frozen core orbitals. The FC Hamiltonian acts only on the subspace spanned by the canonical valence and virtual orbitals. Therefore only the valence electrons are correlated, while the core-valence interactions appear as one-body operators which eliminate the core electrons from the calculation.

A similar approximation using valence-only pseudopotential (PP) Hamiltoni-

ans also invokes this partitioning. In QMC calculations, the most commonly used form is atomic pseudopotentials which are usually constructed for reference atomic configurations. However, transferring the PP across many target systems can be challenging, and achieving systematic accuracy can be difficult. The FC approach offers a significant simplification and it still retains all the advantages of using PPs, while like the PP approach, it also changes the energy scale, which reduces statistical and time-step errors, reducing transferability errors.

Recently FC approximation was implemented in AFQMC and tested its performance across many systems. The frozen core approach shows significant computational savings, compared to fully correlating all the electrons in the system. The detailed result of the tests can be found in Ref. 83.

4.1.2 Frozen Localized Orbitals

The frozen-orbital approach can be generalized to other ways of partitioning the Hilbert space into active and inactive regions. In molecular and condensed matters physics, for example, the active region may sometimes be identified spatially. This active region corresponds to a localized region where the effect of strong electron correlation affects a relatively small number of atoms, while the rest of the system can be treated with a lower level of theory. Various theories of partitioning or embedding [90–94] have been developed to exploit this locality and reduce computational cost. Localized orbital transformations obtained from Foster-Boys [95] or Wannier [96, 97] methods can also be used to achieve more efficient AFQMC calculations.

Recently we have employed the Foster-Boys method for orbital localization, as implemented in NWCHEM [98], to allow direct AFQMC calculations on large system

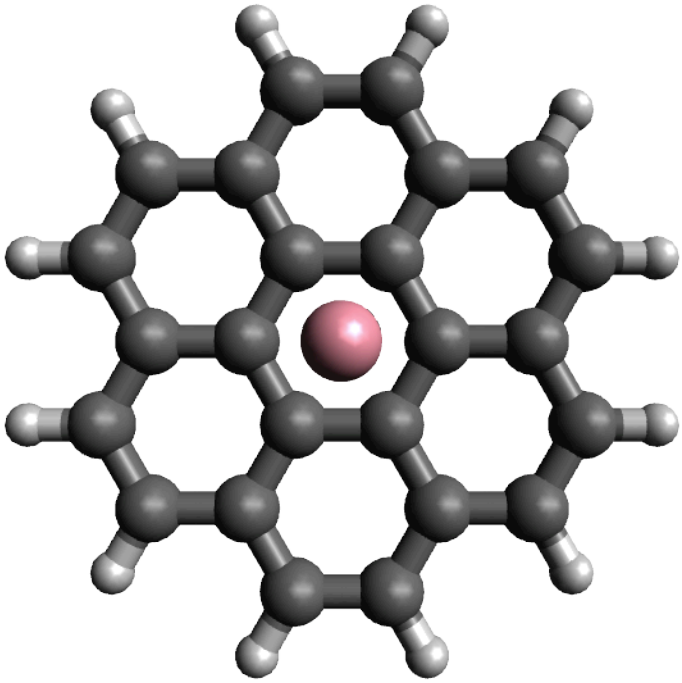

FIG. 4.1: Co atom on coronene ($Co/C_{24}H_{12}$). The red, black, and white balls denote cobalt, carbon, and hydrogen atoms, respectively.

sizes. In the frozen-orbital AFQMC approach, the molecular orbitals of the cluster, which are obtained from Hartree-Fock, are transformed into localized orbitals. We applied this localization approach to Co on coronene ($Co/C_{24}H_{12}$) system as shown in Fig. 4.1 [34]. In this system, strong electron-electron correlations are expected to be spatially localized in the immediate vicinity of the Co atom. Therefore, the orbitals that belong to the atoms far away from Co atom can be frozen in AFQMC calculation.

For $Co/C_{24}H_{12}$, the Foster-Boys localization produces orbitals that are localized on the bonds between atoms. With AFQMC calculations, we systematically study the change in the binding energy of this system as more and more bonds are frozen. The most tightly bound core states, $Co(1s, 2s, 2p)$ and $C(1s)$, were always frozen in AFQMC calculations. Table 4.1 summarizes the result of the study for $h = 1.7$ Å and $h = 3.5$ Å, where h is the distance between Co atom and $C_{24}H_{12}$. The Co

TABLE 4.1: Calculated binding energies of Co on $C_{24}H_{12}$ with AFQMC at two heights near the local minima as a function of the number of orbitals frozen. The Co electronic configurations at $h = 1.7$ Å and $h = 3.5$ Å, are high-spin $3d^8 4s^1$ and high-spin $3d^7 4s^2$ states, respectively.

Bonds Frozen	Binding Energy (eV)	
	$h = 1.7$ Å	$h = 3.5$ Å
No Bonds Frozen	0.42(6)	−0.16(6)
12 C-H bonds	0.44(5)	−0.18(5)
12 C-H + 6 outermost C-C bonds	0.43(5)	−0.24(4)
12 C-H + 18 outermost C-C bonds	0.63(3)	−0.21(3)
12 C-H + 24 outermost C-C bonds	1.45(3)	−0.01(3)

electronic configurations at $h = 1.7$ Å and $h = 3.5$ Å, are high-spin $3d^8 4s^1$ and high-spin $3d^7 4s^2$ states, respectively. The Co, C, and H atoms used cc-pVDZ, 6-31g, and STO-2G basis sets, respectively. For $h = 1.7$ Å, all C-H bonds and 6 outermost C-C bonds can be frozen while introducing essentially no error in the binding energy. For $h = 3.5$ Å, the next 12 outermost C-C bonds can further be frozen with basically no effect in the binding energy. This approach greatly extends the system size that can be treated with AFQMC calculations.

4.2 Modified Cholesky Decomposition: Removing a Preprocessing Computational Bottleneck

The decomposition of the two-body interaction term in Eq. (3.7), which is a preprocessing step and done only once at the beginning of the calculation, is not

unique. This flexibility can be exploited to obtain better performance of the GTO-AFQMC calculation. The straightforward approach to decompose the two-body interaction term is by diagonalizing the two-body matrix directly. However, the direct diagonalization approach scales poorly with the system size and causes computational bottleneck for large systems. We have implemented modified Cholesky decomposition (mCD) in GTO-AFQMC to decompose the two-body interaction matrix [78]. This approach provides much better computational scaling compared to direct diagonalization as illustrated later.

The two-body interaction matrix elements V_{ijkl} in Eq. (3.1) can be expressed as electron-electron Coulomb repulsion integrals (ERIs) in electronic structure calculations

$$V_{ijkl} = \int d\mathbf{r}_1 d\mathbf{r}_2 \, \chi_i^*(\mathbf{r}_1)\chi_j^*(\mathbf{r}_2)\frac{e^2}{|\mathbf{r}_1 - \mathbf{r}_2|}\chi_l(\mathbf{r}_1)\chi_k(\mathbf{r}_2)\,, \tag{4.4}$$

where the GTO basis functions are real. With M basis functions, the size of the symmetric ERI supermatrix $V_{\mu(i,l),\nu(j,k)}$ is $M^2 \times M^2$ where $\mu \equiv (i,l)$ and $\nu \equiv (j,k)$ are compound indices. With direct diagonalization approach, the eigenvalues λ_γ and eigenvectors $X^\gamma_{\mu(i,l)}$ of the symmetric $V_{\mu\nu}$ supermatrix can be obtained and the HS one-body operators in Eq. (3.7) are given by

$$\hat{v}_\gamma = \sqrt{-\lambda_\gamma}\sum_{i,l} X^\gamma_{\mu(i,l)} c_i^\dagger c_l\,. \tag{4.5}$$

The direct diagonalization approach gives $\mathcal{O}(M^6)$ and $\mathcal{O}(M^4)$ scalings of computer time and storage, respectively. The scalings lead to a computational bottleneck for treating large system sizes.

In practice, however, the number of eigenvalues that are significant ($> 10^{-8} E_\mathrm{h}$)

scales only as $\mathcal{O}(M)$. This suggests that the information content in the two-body matrix is only $\mathcal{O}(M)$ and more efficient approaches can be used to decompose the matrix. We have chosen to implement Cholesky decomposition [99–101] approach to carry out the HS decomposition in AFQMC. The decomposition is a modified Cholesky decomposition since the ERI matrix is positive semidefinite instead of positively definite. This method provides a single threshold parameter δ which determines the maximum error in the Cholesky decomposition. This error can be controlled and reduced to zero or within machine precision. In practice, we use δ in the range 10^{-6} to $10^{-4}E_{\mathrm{h}}$, depending on the target statistical accuracy in the AFQMC calculation.

4.2.1 Implementation of Cholesky Decomposition

The Cholesky representation of the symmetric positive semidefinite ERI supermatrix $V_{\mu\nu}$ [100, 101] is given by

$$V_{\mu\nu} = \sum_{j=1}^{J} L_{\mu}^{j} L_{\nu}^{j} + \Delta_{\mu\nu}^{(J)} \,, \tag{4.6}$$

where L_{μ}^{j} $(j = 1 \ldots J)$ are the Cholesky vectors and $\Delta_{\mu\nu}^{(J)}$ is the residual error at the Jth iteration. The $(J+1)$th Cholesky vector is obtained from

$$L_{\mu}^{J+1} = \frac{\Delta_{\mu[\nu]_J}^{(J)}}{\sqrt{\Delta_{[\nu]_J[\nu]_J}^{(J)}}} \,, \tag{4.7}$$

where $[\nu]_J$ denotes the index of the largest diagonal element, $\Delta_{[\nu]_J[\nu]_J}^{(J)}$, of the residual error matrix in the Jth iteration. This iteration is repeated until the stop criterion, $\Delta_{[\nu]_J[\nu]_J}^{(J)} < \delta$, is achieved. This procedure guarantees that all the residual matrix

elements are less than δ:

$$\left|V_{\mu\nu} - V_{\mu\nu}^{(N_{\mathrm{CD}})}\right| = \left|\Delta_{\mu\nu}^{(N_{\mathrm{CD}})}\right| \leq \delta \tag{4.8}$$

where N_{CD} represents the number of Cholesky vectors corresponding to this δ. Damped prescreening [101] is also implemented in each iteration. The damping prevents the decomposition from becoming numerically unstable due to rounding errors.

After the Cholesky decomposition, Eq. (3.7) can be rewritten as

$$\begin{aligned}\hat{V} = \frac{1}{2}\sum_{\gamma=1}^{N_{\mathrm{CD}}}\left(\sum_{il} L_{\mu(i,l)}^{\gamma} c_i^\dagger c_l\right)\left(\sum_{jk} L_{\nu(j,k)}^{\gamma} c_j^\dagger c_k\right) \\ - \frac{1}{2}\sum_{\gamma=1}^{N_{\mathrm{CD}}}\sum_{ijk} L_{\mu(i,j)}^{\gamma} L_{\nu(j,k)}^{\gamma} c_i^\dagger c_k + \mathcal{O}\left(\delta\right) \,,\end{aligned} \tag{4.9}$$

where the extra one-body operator is also explicitly expressed in terms of the Cholesky vectors. The HS one-body operators can be expressed in terms of the Cholesky vectors as

$$\hat{v}_\gamma = \sqrt{-1}\sum_{il} L_{\mu(i,l)}^{\gamma} c_i^\dagger c_l \,. \tag{4.10}$$

The number of auxiliary is given by N_{CD}.

In practice, there are errors in the calculated ERIs and the supermatrix $V_{\mu\nu}$ is not strictly positive semidefinite. In a test case with $M = 180$, we observe from direct diagonalization of $V_{\mu\nu}$ that there are some negative eigenvalues of $\mathcal{O}\left(-10^{-8}\right)$. In this case, Eq. (4.8) will be violated when δ is driven below 10^{-8}. Therefore it is necessary that the most negative eigenvalue of the ERI supermatrix $V_{\mu\nu}$ is smaller (by magnitude) than δ.

4.2.2 Accuracy and Timing Illustrations of mCD

Table 4.2 compares the accuracy of GTO-AFQMC total energies for $Ca^{+}-4H_2$ system using mCD with that using direct diagonalization (DD) of the supermatrix $V_{\mu\nu}$. The detailed parameters of the system and calculation can be found in Ref. 78 For δ ranging from 10^{-8} to 10^{-3}, the AFQMC total energies from mCD are equivalent to each other within statistical uncertainty, and these energies agree with that from DD. The error $E_{\mathrm{mCD}}(\delta) - E_{\mathrm{DD}}$ from Table 4.2 is plotted in Fig. 4.2. For comparison, the corresponding error in the unrestricted Hartree-Fock (UHF) variational energy, computed using the same set of Cholesky vectors, is also shown in Fig. 4.2 and is seen to correlate well with the error in the AFQMC energy.

The timing comparison of DD vs. mCD methods is illustrated in Fig. 4.3. The computational details can be found in Ref. 78. As expected, the CPU time scaling of the DD method scales approximately as M^6. The mCD algorithm with prescreening scales only as $\sim M^3$. This improvement is highly important for treating systems with large basis sets efficiently. For the largest basis ($M = 827$) reported in Ref. 78, mCD required less than 6 hours on a single core machine, while DD could have taken more than 92 days and nearly 1 TB of memory, were it available, on the same computer.

Our current implementation of mCD has not exploited the sparsity of the Cholesky vectors. The memory required to store the Cholesky vectors currently scales as $\mathcal{O}(M^3)$. The memory requirement can be further reduced to $\mathcal{O}(M^2)$ by fully exploiting the sparse structure of the Cholesky vectors [100].

TABLE 4.2: GTO-AFQMC total energies for several values of the mCD threshold parameter δ for $Ca^{+}-4H_2$ with $M = 155$. The total energy E_{DD}, obtained from direct diagonalization of $V_{\mu\nu}$, is presented for comparison; the eigenvalue cutoff is also shown. N_γ is the corresponding number of auxiliary-fields. A full rank, symmetric, positive definite $V_{\mu\nu}$ matrix would have required $155^2 = 24025$ Cholesky vectors. All energies are in E_{h}.

Direct diagonalization		
$V_{\mu\nu}$ eigenvalue cutoff	E_{DD}	N_γ
$\lambda_\gamma > 2 \times 10^{-8}$	−681.42990(20)	2280
Modified CD		
Cholesky δ	E_{mCD}	N_{CD}
10^{-8}	−681.43007(15)	1727
10^{-6}	−681.43003(17)	1120
10^{-5}	−681.42988(20)	850
10^{-4}	−681.42977(18)	643
10^{-3}	−681.42932(19)	511
2×10^{-3}	−681.42991(19)	468
3×10^{-3}	−681.43102(18)	436
3.5×10^{-3}	−681.42958(19)	425
4×10^{-3}	−681.39679(19)	403
5×10^{-3}	−681.39609(17)	379

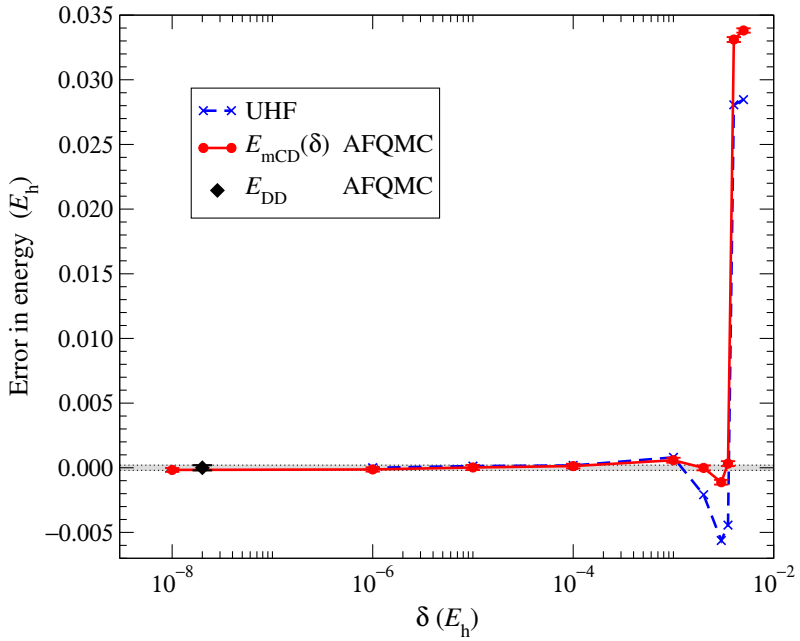

FIG. 4.2: AFQMC total energy error, $E_{\mathrm{mCD}}(\delta) - E_{\mathrm{DD}}$, as a function of the mCD threshold parameter δ (energies are given in Table 4.2). The width of the gray line indicates the statistical uncertainty of E_{DD}. The corresponding error (with respect to the UHF energy) of the trial wave function variational energy is also shown.

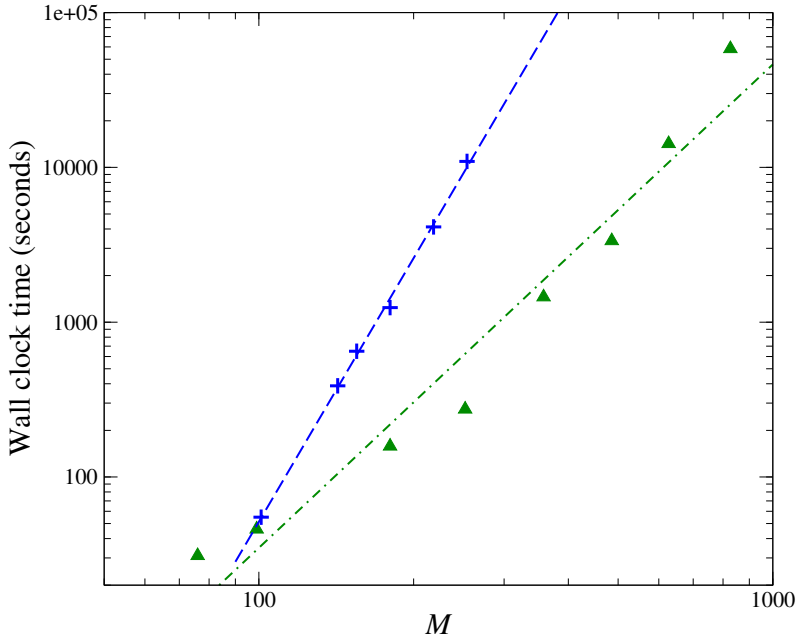

FIG. 4.3: Log-log plots of wall clock times (seconds) vs. basis size M, comparing DD (+) and mCD (▲) of the ERI supermatrix $V_{\mu\nu}$. The dashed (dashed-dotted) lines are linear regressions. The DD slope $\sim M^{5.7}$ is consistent with the expected M^6 scaling, while mCD scales as $\sim M^{3.1}$.

CHAPTER 5

Co Adatoms on Graphene

Graphene, with its unique band structure at the Dirac point and exceptional physical properties, has the potential to revolutionize electronics technology [2, 4, 5, 13]. Moore's law observes that the density of transistors on an integrated circuit doubles approximately every two years [102]. However, silicon and other existing transistor materials are considered approaching their physical limits [103]. Graphene transistors can potentially run at faster speeds and dissipate heat more efficiently. Graphene can provide a new platform material that would allow the semiconductor technology to continue its march toward ever-smaller and faster electronic devices, extending Moore's law for decades to come [104, 105].

Recently, research interest in the adsorption of transition metal adatoms on graphene has grown rapidly because of its possible use to induce magnetism on graphene for spintronic applications [10–13]. Single Co atoms on graphene have been extensively studied, both theoretically [19–34] and experimentally [35–42]. For example, scanning tunneling microscopy (STM) experiments have demonstrated the ability to controllably ionize a Co adatom on graphene using a back gate voltage

[35]. A high magnetic anisotropy for Co/graphene has been observed [39, 42]. The observation of the Kondo effect caused by Co adatoms on graphene has been reported [41, 42] and theoretical studies show that the Kondo effect can be turned on and off by shifting the Fermi energy [23, 24, 106, 107]. It is thus of great importance to understand the properties of Co/graphene both from a fundamental and applied perspective.

Previous theoretical studies [19–32] of Co adsorption on graphene have shown conflicting results and none of these results is fully consistent with experimental findings. We address the problem from two complementary angles, using auxiliary-field quantum Monte Carlo (AFQMC) calculations. First we apply an exact free-projection AFQMC approach to systematically benchmark the various theoretical methods in a series of model systems which are smaller in size but retain key features of Co/graphene. These results will provide guidance for future studies of transition metal adsorption on graphene, especially in the selection of computationally less costly approaches. Second, a frozen-orbital embedding scheme is developed to extend the system size that can be treated with AFQMC (see Table 4.1). Using the new approach, we determine the relative stability of different adsorption sites and the magnetic states of Co/graphene by direct AFQMC calculations of Co on large substrates (e.g., $C_{24}H_{12}$), augmented by a finite-size correction from the substrate to graphene, treated by density functional theory. Our results are consistent with and provide a quantitative explanation for the observations from recent STM experiments of Co adatoms adsorbed on H-intercalated graphene/SiC(0001) [38].

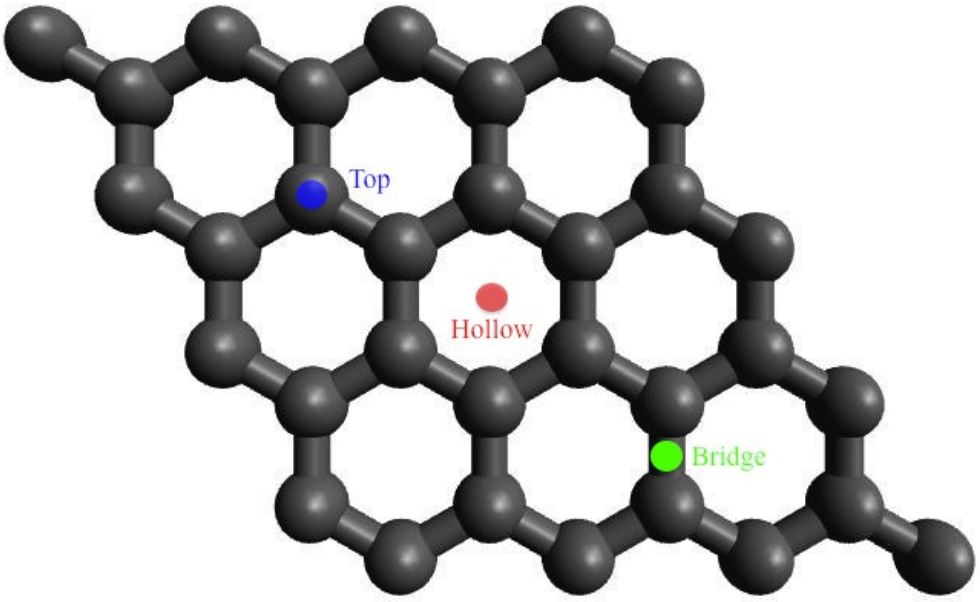

FIG. 5.1: The three high-symmetry Co adsorption sites on graphene referred as hollow, bridge, and top sites which describe a Co atom right above the center of the hexagonal ring, the middle of a C–C bond, and a carbon atom, respectively. Most DFT calculations predict the hollow site as the global minimum. Experimental studies, however, find that Co atoms can be adsorbed on both the hollow site and the top site.

5.1 Prior Calculations

Previous theoretical studies have been focused on three high-symmetry Co adsorption sites on graphene, as shown in Fig. 5.1, i.e., the hollow, bridge, and top sites which describe a Co atom right above the center of the hexagonal ring, the middle of a C–C bond, and a carbon atom, respectively. Most of these studies have addressed Co adsorption on graphene at the density functional theory (DFT) level, using local or semi-local functionals, or an empirical Hubbard on-site repulsion U (DFT+U) [19–31]. However, the applicability of methods based on independent-electron approximations in such systems is unclear, since electron correlation effects can be significant.

Indeed calculations have reported widely varying results for the nature of the

magnetic state, adsorption site, and binding energy of Co as a function of adsorption height. For example, DFT using the generalized gradient approximation (GGA) [43] shows [19–31] that the sixfold hollow site is the global minimum, with an equilibrium height of $h_{\mathrm{eq}} \sim 1.5$ Å and a low-spin $3d^9 4s^0$ Co atom configuration ($S = 1/2$). A different functional, the hybrid Becke three-parameter Lee-Yang-Parr (B3LYP) [44], predicts [24] an equilibrium height of $h_{\mathrm{eq}} \sim 1.9$ Å with a high-spin $3d^8 4s^1$ configuration ($S = 3/2$) at the hollow site. Results from the GGA+U approximation [45, 46] have shown sensitivity to the value of the parameter U chosen. For $U = 2$ eV, it predicts the global minimum to be the hollow site with a low-spin configuration, while for $U = 4$ eV, the global minimum is the top site with a high-spin configuration [23, 27, 31]. A perturbative quantum chemistry calculation based on a complete active space self-consistent field (CASSCF) [47] reference predicts the global minimum at the van der Waals (vdW) region with $h_{\mathrm{eq}} \sim 3.1$ Å and a high-spin $3d^7 4s^2$ configuration [32]. The contrasting results underscore the need for better understanding of and fundamentally more accurate approaches to treat transition metal adsorption on graphene.

Most DFT calculations predict the hollow site as the most favorable adsorption site for Co/graphene. Using phaseless AFQMC, we had determined [33] that bonding at the hollow site, different from the DFT predictions, exhibited a double-well structure with nearly equal binding energy. Recently, however, experimental studies have indicated that single Co atoms can be adsorbed on both the hollow site and the top site [37–39]. Motivated by these experimental results, we investigate the binding energy and electronic properties of Co/graphene for all three high-symmetry adsorption sites [34].

5.2 Benchmarking DFT, CCSD(T), and AFQMC

Before we address Co adsorption on graphene, first we apply an exact free-projection AFQMC approach to systematically benchmark the various theoretical methods in a series of model systems which are smaller in size but retain key features of Co/graphene. The three model systems are Co/C_6H_6, Co/C_2H_4, and Co/C_4H_8, which represent prototypes of the three high-symmetry adsorption sites in Co/graphene, as shown in Fig. 5.2. These FP-AFQMC results are used to benchmark DFT, with local and hybrid functionals, DFT+U, CCSD(T), and phaseless AFQMC. The C–C bond length in the model systems was fixed to that of graphene, 1.42 Å, and the C–H bond length was set to 1.09 Å, which is close to the experimental bond lengths in the three molecules.

In the mean field calculations, we employ Gaussian basis sets for DFT, hybrid DFT, and HF, which were performed with NWCHEM [98]. DFT+U calculations were done with the PWSCF code of the QUANTUM ESPRESSO package [108], using planewaves and ultrasoft pseudopotentials[1], with a 50 Ry kinetic energy cutoff and a charge density cutoff of 400 Ry. Each of the three model systems, the substrate molecules, and the Co atom were treated using a 15 Å cubic supercell with single k-point sampling.

The AFQMC calculations also used standard Gaussian basis sets and a frozen-core approximation [83], thus avoiding the need for pseudopotentials; only the most tightly bound core states were frozen: Co($1s, 2s, 2p$) and C($1s$). Typical AFQMC runs used $\simeq$ 5000 walkers and a Trotter time step $\Delta\tau = 0.01$ Ha^{-1}, and final results were extrapolated to the $\Delta\tau \to 0$ limit. The FP-AFQMC results are in

[1]The pseudopotentials were obtained from http://www.quantum-espresso.org; H.pbe-rrkjus.UPF, C.pbe-rrkjus.UPF, and Co.pbe-nd-rrkjus.UPF for GGA calculations and H.pz-rrkjus_psl.0.UPF, C.pz-n-rrkjus_psl.0.UPF, and Co.pz-nd-rrkjus.UPF for LDA's.

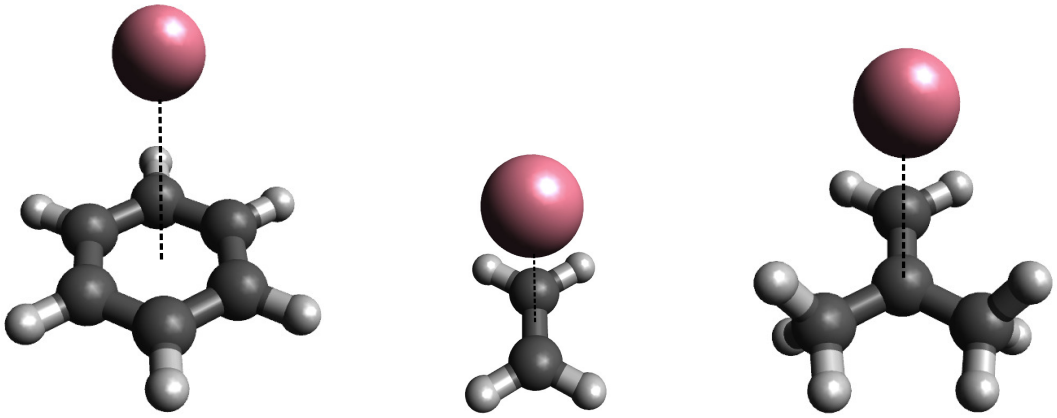

(a) (b) (c)

FIG. 5.2: Three model systems represent prototypes of the three high-symmetry adsorption sites in Co/graphene: the sixfold hollow site, the twofold bridge site, and the top site. These model systems are used to systematically benchmark various DFT methods, CCSD(T), and phaseless AFQMC. (a) Co atom on C_6H_6. (b) Co atom on C_2H_4. (c) Co atom on C_4H_8.

principle independent of the trial wave function, although the quality of Ψ_T affects the convergence time and statistical accuracy. The computational cost scales with the number of determinants in a multi-determinant Ψ_T [80]. Single-determinant HF Ψ_T was found to be sufficient for high-spin states, while multi-determinant Ψ_T obtained from CASSCF was found to be more efficient for low-spin states. All phaseless AFQMC results used single-determinant unrestricted Hartree-Fock (UHF) Ψ_T.

Care was taken to remove finite basis set error in the AFQMC results. The following basis sets[2] were used in AFQMC calculations. The Co atom used the correlation-consistent core-valence cc-pwCVTZ basis set, where "core" refers to the Co $3s, 3p$ semicore states. For C and H atoms, valence-only cc-pVTZ and cc-pVDZ were used, respectively. For several geometries near the minima, the Co(cc-

[2]We use the correlation-consistent polarized weighted core-valence (cc-pwCVxZ) and the correlation-consistent polarized valence (cc-pVxZ) basis sets, where x = D, T, and Q for double, triple, and quadruple zeta, respectively.

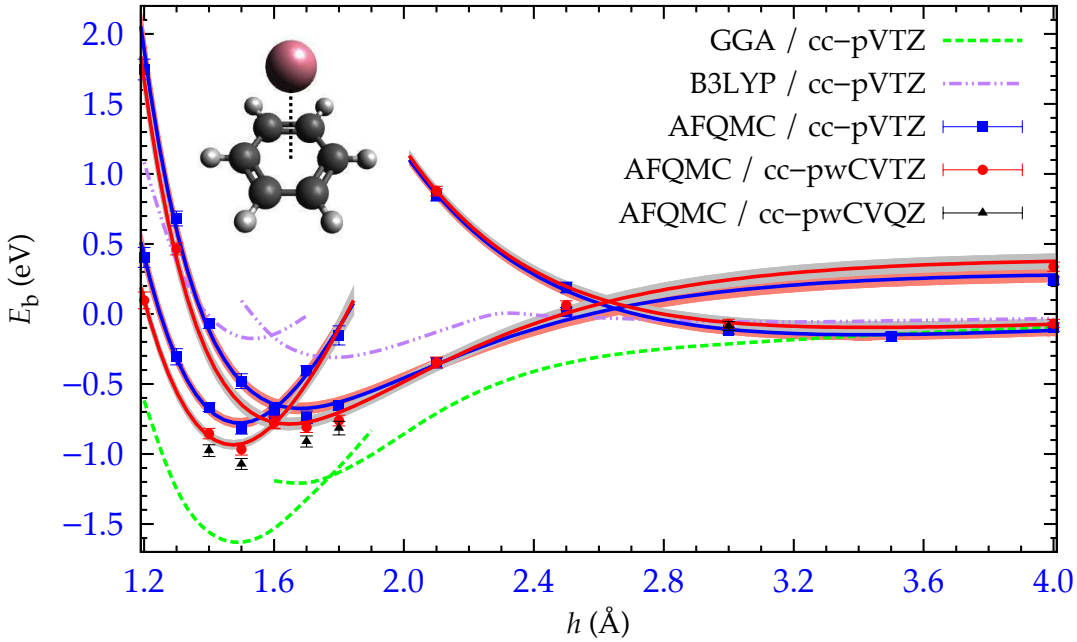

FIG. 5.3: Binding energy of Co on C_6H_6 as a function of Co adsorption height h at the six-fold site for GGA, B3LYP, and phaseless AFQMC for various basis sets. For phaseless AFQMC, left, middle, and right curves correspond to nominal $3d^9 4s^0$, $3d^8 4s^1$, and $3d^7 4s^2$ Co configurations, respectively. For GGA and B3LYP the left and right curves correspond to $3d^9 4s^0$ and $3d^8 4s^1$ Co configurations, respectively. The DFT results are converged by the Co(cc-pVTZ) level, while AFQMC is not yet fully converged even at the Co(cc-pwCVQZ) level for small h's. The shaded area on the AFQMC Morse fits reflects one standard deviation which includes both statistical and systematic errors.

pwCVQZ) basis set was used to obtain extrapolation to the complete basis set (CBS) limit. Not surprisingly, while the DFT results are converged by the Co(cc-pVTZ) level, AFQMC is not yet fully converged even at the Co(cc-pwCVQZ) level as shown in Fig. 5.3. To estimate the effect of the CBS extrapolation, we used the procedure in Ref. 109. The CBS extrapolation procedure treats separately the HF total energy and the correlation energy,

$$E_{\mathrm{HF}}(\infty) \approx E_{\mathrm{HF}}(x) - Be^{-\alpha x}\,, \tag{5.1}$$

$$E_{\mathrm{corr}}(\infty) \approx E_{\mathrm{corr}}(x) - \frac{C}{x^3}\,, \tag{5.2}$$

since correlation energy convergence is much slower than the convergence of HF total energy [109–111]. Here, x is the correlation consistent basis cardinal number and α, B, and C are constants. Trotter time step extrapolations were obtained from results for a smaller basis set [cc-pVTZ for Co and cc-pVDZ for C and H] and applied to the results for the larger basis sets.

The Co/C_6H_6 benchmark results in Table 5.1 show that phaseless AFQMC and CCSD(T) produce accurate binding energies for high-spin Co atom configurations ($S = 3/2$) in all three model systems. The binding energies are defined as $E_{\mathrm{b}}(h) \equiv E^{\mathrm{Co/substrate}}(h) - E^{\mathrm{Co}} - E^{\mathrm{substrate}}$, where h is the perpendicular distance between Co atom and the substrate, and the last two terms on the right are the total energies of the isolated Co atom and corresponding substrate, respectively. In the case of the low-spin configuration ($S = 1/2$), both show small errors, with phaseless AFQMC overestimating the binding energy of Co/C_6H_6 by $\sim 0.1\,\mathrm{eV}$ and CCSD(T) underestimating it by approximately the same amount, as shown in Table 5.1.

We also benchmark DFT, with local and hybrid functionals, and DFT+U methods. Figure 5.4 shows the binding energy curves of Co/C_6H_6 as a function of h from

TABLE 5.1: Calculated binding energies of Co on C_6H_6 at three heights near the local minima. All binding energies have been extrapolated to the CBS limit. The uncertainty on AFQMC results includes both statistical and systematic errors and the uncertainty for CCSD(T) results comes from CBS extrapolations.

	Binding Energy (eV)		
	FP-AFQMC	AFQMC	CCSD(T)
$S = 1/2$			
$3d^9 4s^0$ ($h = 1.5$ Å)	$-0.99(4)$	$-1.07(4)$	$-0.91(4)$
$S = 3/2$			
$3d^8 4s^1$ ($h = 1.7$ Å)	$-0.92(4)$	$-0.91(4)$	$-0.95(4)$
$3d^7 4s^2$ ($h = 3.0$ Å)	$-0.15(3)$	$-0.15(3)$	$-0.15(3)$

GGA, B3LYP, GGA+U, in comparison with exact FP-AFQMC results. All energies have been extrapolated to the CBS limit. The FP-AFQMC results show that the ground-state electronic configuration of the Co atom undergoes two transitions as h decreases, which produces three different configurations: high-spin $3d^7 4s^2$, high-spin $3d^8 4s^1$, and low-spin $3d^9 4s^0$ states, respectively. All DFT functionals and DFT+U produce only two ground-state configurations, a high-spin $3d^8 4s^1$ for large h's and a low-spin $3d^9 4s^0$ for small h's. They also incorrectly predict the $3d^8 4s^1$ state as the ground-state configuration for the free Co atom.

Figure 5.5 summarizes the error in the calculated binding energy (near the optimal geometry as determined by FP-AFQMC) from DFT using different functionals for all three model systems. In Co/C_2H_4, the same three nominal ground-state electronic configurations of the Co atom are found as those in Co/C_6H_6. In Co/C_4H_8, however, the low-spin $3d^9 4s^0$ state is unbound, therefore only the high-spin states are considered. We chose a representative set of the most common DFT functionals [57]:

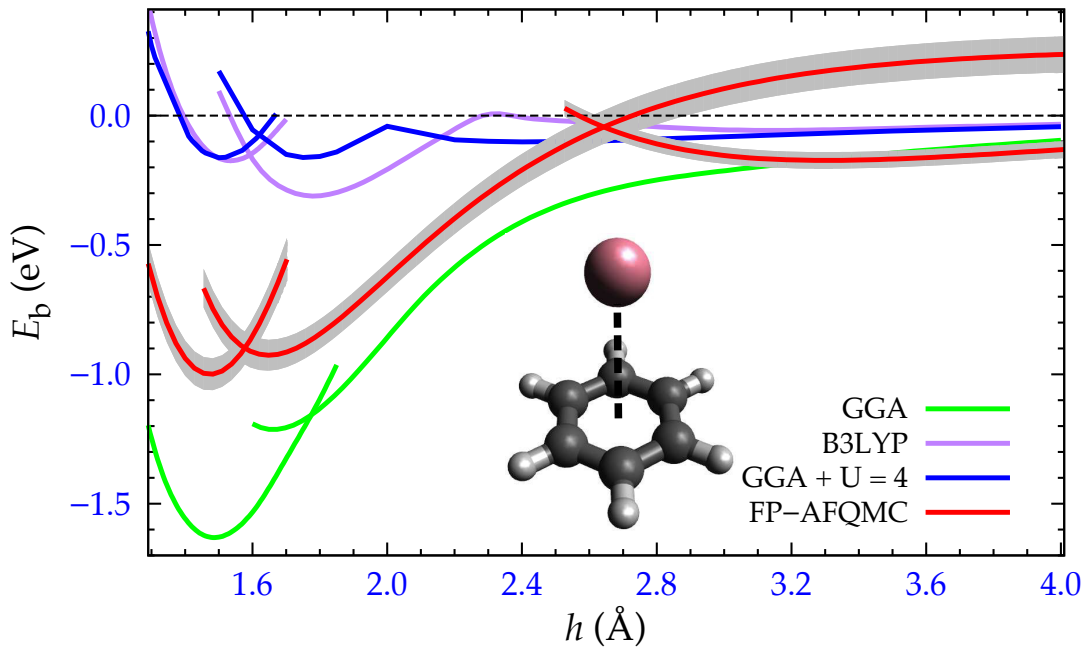

FIG. 5.4: Binding energy of Co on C_6H_6 as a function of Co adsorption height h at the six-fold site for GGA, B3LYP, GGA+U, and exact FP-AFQMC. For FP-AFQMC, left, middle, and right curves correspond to nominal $3d^9 4s^0$, $3d^8 4s^1$, and $3d^7 4s^2$ Co configurations, respectively. For GGA, B3LYP, and GGA+U, the left and right curves correspond to $3d^9 4s^0$ and $3d^8 4s^1$ Co configurations, respectively. The shaded area on the AFQMC Morse fits reflects one standard deviation which includes both statistical and systematic errors.

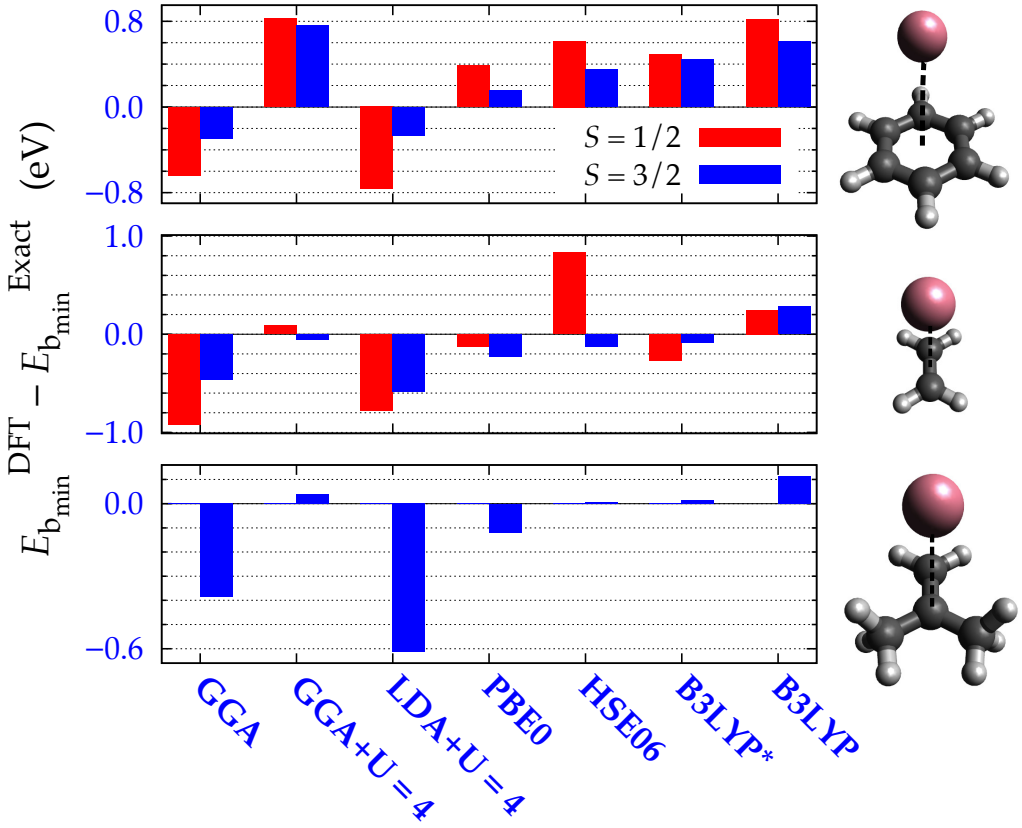

FIG. 5.5: The error in the calculated binding energy from several DFT hybrid functionals, for Co/C_6H_6, Co/C_2H_4, and Co/C_4H_8, respectively. The low-spin ($S = 1/2$) and high-spin ($S = 3/2$) states correspond to $3d^9 4s^0$ and $3d^8 4s^1$ Co configurations, respectively. The results from GGA+U and LDA+U for $U = 4$ eV are also shown for comparison.

the local density approximation (LDA), GGA, the hybrid Perdew-Burke-Ernzerhof (PBE0) [112], the hybrid Heyd-Scuseria-Ernzerhof (HSE06) [113, 114], B3LYP, and a modification for transition metals, B3LYP*. As suggested from Fig. 5.5, none of the functionals gives a uniformly correct description of all three model systems. The hybrid PBE0 and B3LYP* show the best agreement among the DFT functionals.

Two typical DFT+U results are also included for comparison in Fig. 5.5. A more systematic analysis of the accuracy of DFT+U is given in Fig. 5.6, in which we calculate the error in the binding energy as a function of the parameter U. The U values span the range used in Refs. 23, 27, and 31. All DFT+U calculations use the

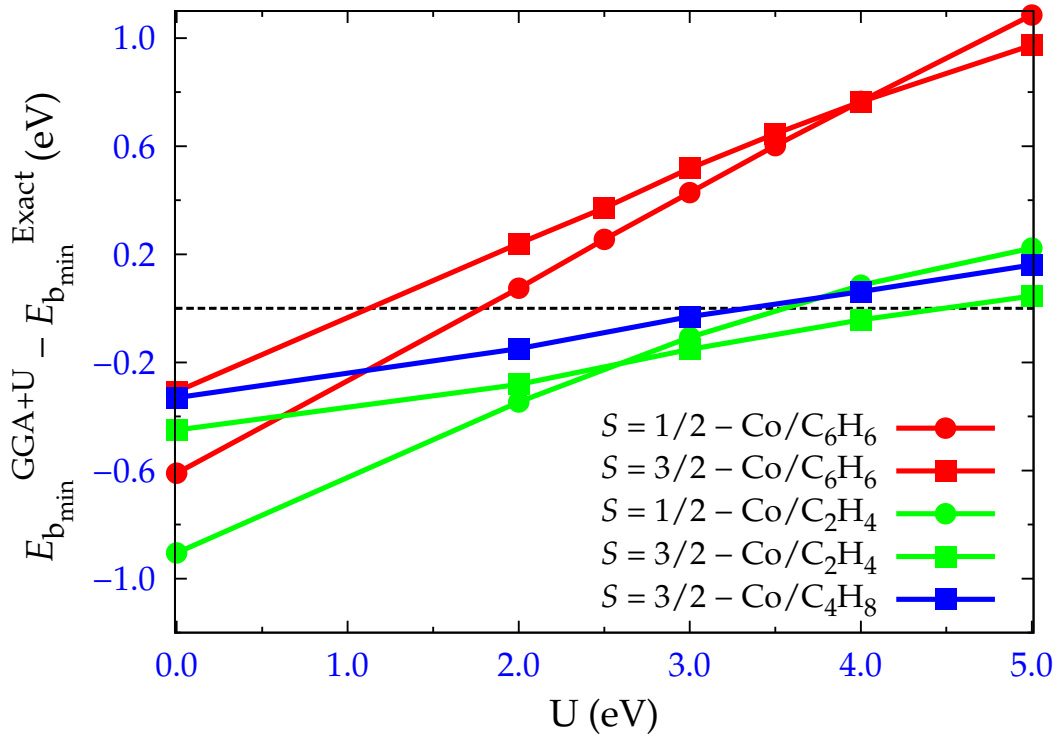

FIG. 5.6: The error in the calculated binding energy from GGA+U as a function of U, for Co/C_6H_6, Co/C_2H_4, and Co/C_4H_8, respectively, at their respective minimum position h. The low-spin ($S = 1/2$) and high-spin ($S = 3/2$) states correspond to $3d^9 4s^0$ and $3d^8 4s^1$ Co configurations, respectively.

same exchange interaction $J = 0.9$ eV. The results suggest that there is no single "correct" value of U that can quantitatively capture the physics of Co adsorption on graphene across the different adsorption sites. For Co/C_6H_6, $U \sim 2$ eV shows good agreement with the exact result, while Co/C_2H_4 and Co/C_4H_8 require larger values, $U \sim 4$ eV.

We have presented direct and systematic benchmark studies of various computational methods for Co/C_6H_6, Co/C_2H_4, and Co/C_4H_8. These benchmark studies can provide guidance for future studies of transition metal adsorption on graphene, especially in the selection of computationally less costly approaches. The results can also assist in improving DFT functionals.

5.3 Properties of Co Adatoms on Graphene

After the benchmark studies, we use frozen-orbital phaseless AFQMC to investigate the stability and electronic properties of single Co adatoms on graphene. Bonding interactions between Co atom and graphene are essentially local and decrease rapidly with distance. Therefore, it is reasonable to consider the graphene near region to model the Co/graphene interaction. Our tests show that, to reach the desired accuracy in predicting the binding energies in Co/graphene, the model systems discussed in previous section are inadequate to be used to model Co/graphene. Instead we use $Co/C_{24}H_{12}$, $Co/C_{10}H_8$, and $Co/C_{13}H_{10}$ to model the hollow, the bridge, and the top sites, respectively. These clusters are illustrated in Fig. 4.1 and Fig. 5.7. Each of these clusters includes, at least, nearest- and next-nearest-neighbor Co–C interactions.

Direct AFQMC calculations on the $Co/C_{24}H_{12}$ cluster are very expensive computationally. However, as discussed in the previous chapter (section 4.1.2), the Hartree-Fock orbitals localized on atoms far away from Co atom can be frozen in AFQMC calculation. Thus we employ the frozen-orbital approximation where the C–H bonds and the outermost C–C bonds are frozen. While this approximation reduces significantly the number of electrons needed to be treated with AFQMC, it essentially introduces no error in the calculated binding energies (see Table 4.1).

Since strong electron-electron interactions are expected to be spatially localized in the immediate vicinity of the Co atom, residual size corrections are small. To capture these, we use a size-correction embedding scheme [90]. The size corrections are treated using a lower level of theory like DFT. After size correction, the binding

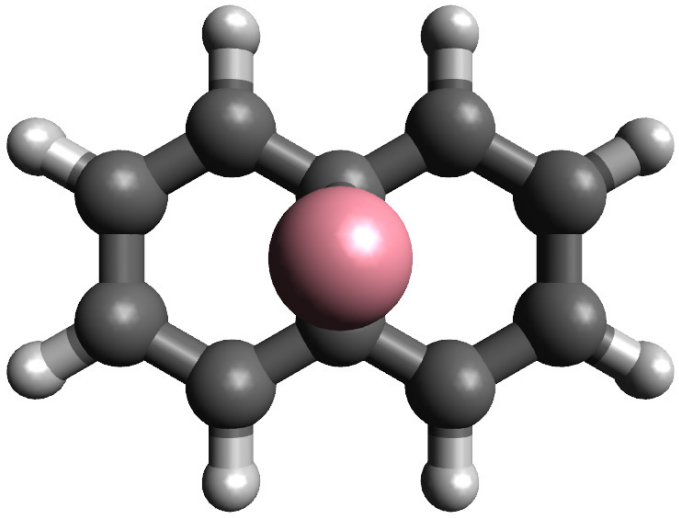

(a)

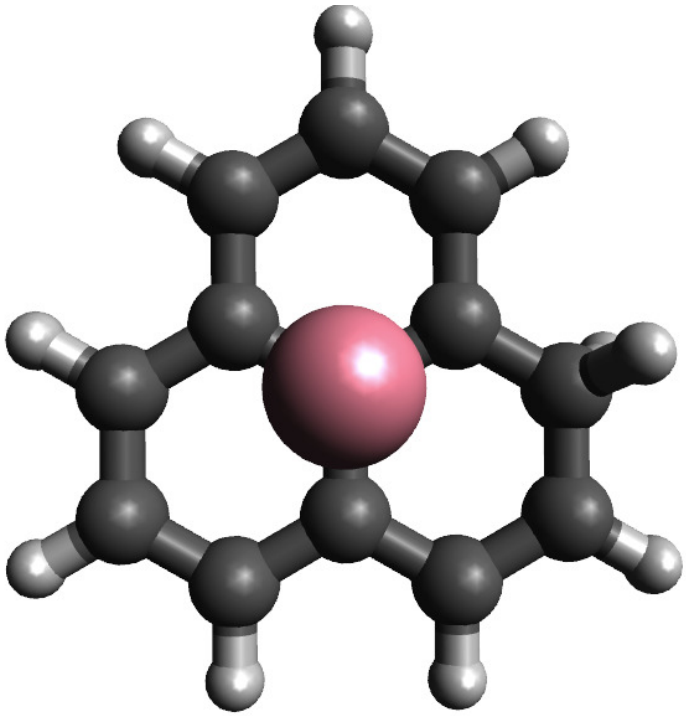

(b)

FIG. 5.7: The clusters used to model interaction between Co atom and graphene at the bridge site and the top site. (b) Co atom on $C_{10}H_8$. (c) Co atom on $C_{13}H_{10}$. Each cluster includes, at least, nearest- and next-nearest-neighbor Co–C interactions.

energy of the high level theory is given by

$$E_{\mathrm{b}}^{\mathrm{Co/graphene}} = E_{\mathrm{b,\ Many\text{-}body}}^{\mathrm{Co}/z} + (E_{\mathrm{b,\ DFT}}^{\mathrm{Co/graphene}} - E_{\mathrm{b,\ DFT}}^{\mathrm{Co}/z}), \tag{5.3}$$

where z denotes the near region's substrate and geometry (e.g. $\mathrm{Co/C_{24}H_{12}}$) . The binding energy is calculated as a function of height h for each spin state of the Co atom. The C–C bond length for each substrate was again fixed to that of graphene, 1.42 Å. The C–H distance to the terminating H atoms was set to 1.09 Å. Previous studies have shown little sensitivity to the terminating H bond distance [115]. All AFQMC calculations were all done for fixed substrate geometries. We will consider the effect of substrate geometry relaxation with the assistance of DFT calculations, as discussed later.

To obtain the Co/graphene DFT binding energy $E_{\mathrm{b,\ DFT}}^{\mathrm{Co/graphene}}$ of a single Co atom on graphene, a large graphene supercell was used. We used GGA as implemented in the PWSCF code of the QUANTUM ESPRESSO package [108], with periodic boundary conditions and ultrasoft pseudopotentials. A 5×5 in-plane supercell was used, which contains 50 C atoms and a Co atom. The artificial supercell periodicity also introduces another finite-size effect, but this can be easily checked by increasing the supercell size. Previous calculations have shown that 5×5 reduces finite-size effect to less than 0.01 eV in the binding energy. The in-plane lattice parameter was 12.3 Å and the out-of-plane distance perpendicular to the nearest image graphene plane was set to 15 Å. A planewave basis kinetic energy cutoff of 50 Ry and a charge density cutoff 400 Ry were used for all geometries. The Brillouin-zone sampling used a Γ-centered $4 \times 4 \times 1$ k-point grid and a Gaussian smearing width of 0.04 eV is used for the electronic occupations.

We examined the substrate relaxation effect by comparing the relaxed and

unrelaxed 5×5 PWSCF supercell results and including it as an additional size-correction layer. For this purpose, the C atoms nearest to the Co atom in the relaxed substrates were allowed to relax only in the in-plane direction. The value of h was defined in relation to these atoms, and the remainder of the C atoms were completely relaxed in C_{2v} symmetry for the hollow and the bridge sites, and in C_{3v} symmetry for the top site. Relaxation was considered complete when the force on all atoms, except the restricted atoms, was less than 0.02 eV/Å. Substrate relaxation lowers the binding energy by $\sim 0.05\,\text{eV}$ for the hollow site and $\sim 0.02\,\text{eV}$ for the bridge and the top sites near the minima.

It is reassuring to note that the size correction in Eq. (5.3) is essentially independent of the choice of DFT exchange-correlation functional. This insensitivity is illustrated, for GGA and B3LYP, in Fig. 5.8, using Co/C_6H_6 with $Co/C_{24}H_{12}$ as the reference substrate (B3LYP calculations for the 5×5 supercell were time consuming and difficult to converge). As Fig. 5.8 illustrates, while GGA and B3LYP show large differences between their binding energy curves, the size correction in Eq. (5.3) is essentially independent of which is used. We have also checked the size correction with other DFT functionals and DFT+U, and all the test showed a similar insensitivity. For the clusters in Fig. 4.1 and Fig. 5.7, the finite-size corrections were all less than 0.1 eV near the minima and within 0.03 eV of each other.

The final binding energy curves of Co/graphene for all three sites are shown in Fig. 5.9. All results are obtained with AFQMC except for the bridge site which is provided by CCSD(T). Several CCSD(T) calculations are also done for the vdW region and the top site and they agree with AFQMC results, consistent with the benchmark results earlier. The lines in Fig. 5.9 are Morse fits [116] to the AFQMC and CCSD(T) results. The size correction is not applied to the vdW region because the chosen DFT functionals did not include vdW interactions (see Ref. 117,

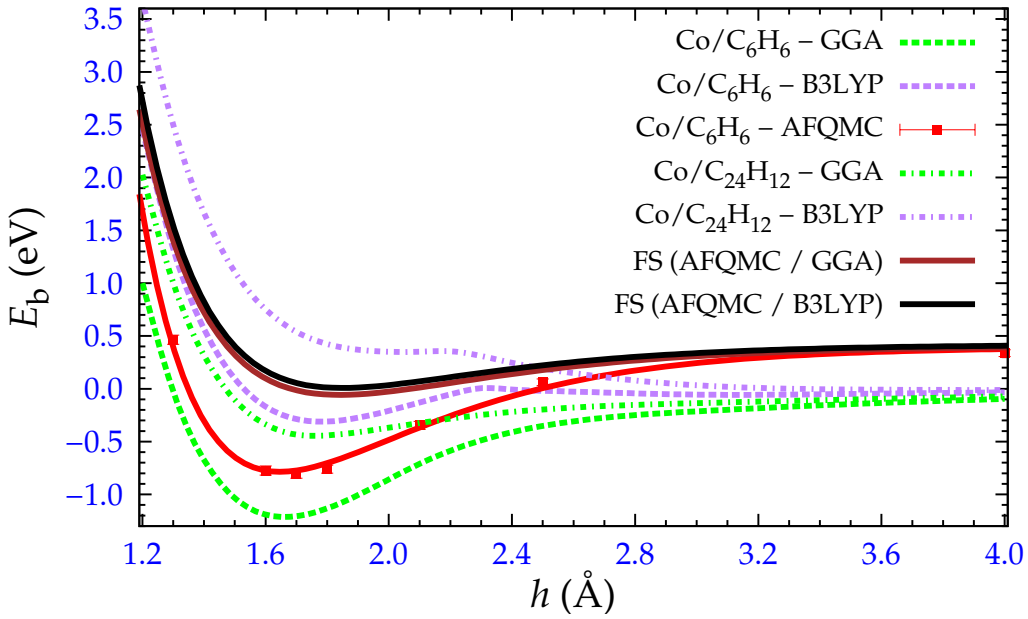

FIG. 5.8: Finite-size (FS) corrections and the binding energies of Co/C_6H_6 and $Co/C_{24}H_{12}$ systems in the high-spin $3d^8 4s^1$ state. The two FS curves are basically identical and show insensitivity to the choice of DFT flavors. The corrections are applied to the $3d^8 4s^1$ AFQMC binding energy curve of Co/C_6H_6 with cc-pwCVTZ basis set. Similar independence on DFT functional is found for the other spin states.

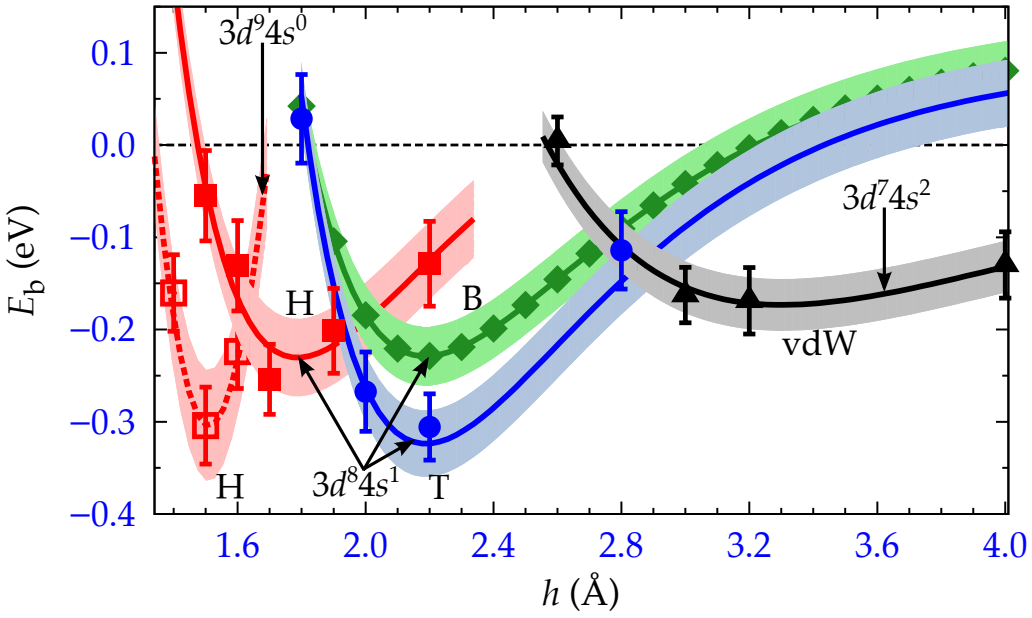

FIG. 5.9: Binding energy of Co on graphene as a function of h for all three sites. Squares, diamonds, circles and triangles correspond to hollow (H), bridge (B) and top (T) sites, and the vdW region, respectively. The dashed line indicates the low-spin $3d^9 4s^0$ hollow site (open squares). Extrapolation to the CBS limit has been included. Shaded areas are one-σ estimates of uncertainties, including the statistical errors in AFQMC.

for example). Indeed, with the standard functionals used here, the vdW region becomes unbound after size-correction is applied [33]. The vdW binding energy curve in Fig. 5.9 is expected to be free of finite-size errors and nearly exact, however, since both AFQMC and CCSD(T) calculations show Co/C_6H_6 to be close to $Co/C_{24}H_{12}$, $Co/C_{10}H_8$, and $Co/C_{13}H_{10}$, which give essentially the same binding energy, as discussed later. For reference, we also show the low-spin $3d^9 4s^0$ hollow-site curve (dashed line) obtained from earlier phaseless AFQMC calculations [33], after correcting the phaseless bias with the FP results of Table 5.1. Because of energy barriers, this curve will not be relevant to the energetics, as discussed below.

Multiple energy minima are seen in Fig. 5.9, associated with different adsorption sites and different spin states. However, a closer examination of the energetics shows that the Co atom can only occupy the vdW region (all sites) at $h \sim 3.3$ Å and the top site at $h \sim 2.2$ Å. The binding energy at the vdW region is ~ -0.18 eV, while that at the top site is ~ -0.31 eV. Although the bridge site and hollow sites are also bound in the nominal $3d^8 4s^1$ configuration, they are either metastable or inaccessible in the adsorption process. Test calculations for $Co/C_{13}H_{10}$ indicate that the bridge site is a saddle point, unstable to Co relaxing to the top site. The minimum for the hollow site lies at smaller $h \sim 1.7$ Å. The kinetic barrier between it and the top site is ~ 0.13 eV, which is large compared with the temperatures (8 to 20 K) at which the experiments are performed [35, 37–40]. Energetically, the Co atom is prevented, therefore, from hopping to the inner hollow site. In contrast, the barrier height between the vdW region and the top site is much smaller.

5.4 Binding Energy at vdW Region

Extra care was required when using a DFT finite-size correction at the vdW region of Co/graphene. It is well known that standard DFT functionals poorly capture dispersive interactions [118]. Consequently, the size correction from DFT at the vdW region might lead to an error. In addition, all the DFT functionals chosen here predict incorrectly the ground-state configuration of the free Co atom. This further indicates that using DFT for a finite-size correction at this region could be unreliable.

To address this issue, we calculate the binding energies of Co/C_6H_6, $Co/C_{10}H_8$, $Co/C_{13}H_{10}$, and $Co/C_{24}H_{12}$ at the vdW region with AFQMC and CCSD(T). Figure 5.10 summarizes the binding energies of these clusters. In these calculations, we use cc-pwCVQZ, cc-pVDZ, and cc-pVDZ basis sets for Co, C, and H atoms, respectively. The CBS correction for this basis set is very small at this region and the results can be considered converged within error bar. Although the sizes of the clusters are quite different, all clusters produce essentially the same binding energy. This indicates that the vdW region is free of finite-size errors.

As we mentioned above, the size correction is not applied to the vdW region in Fig. 5.9. In fact, if the size correction is applied, the vdW region becomes unbound [33]. The van der Waals density functional methods [119, 120], which include dispersions in an approximate way, might give a better finite-size correction. Further investigations will be required to examine these functionals.

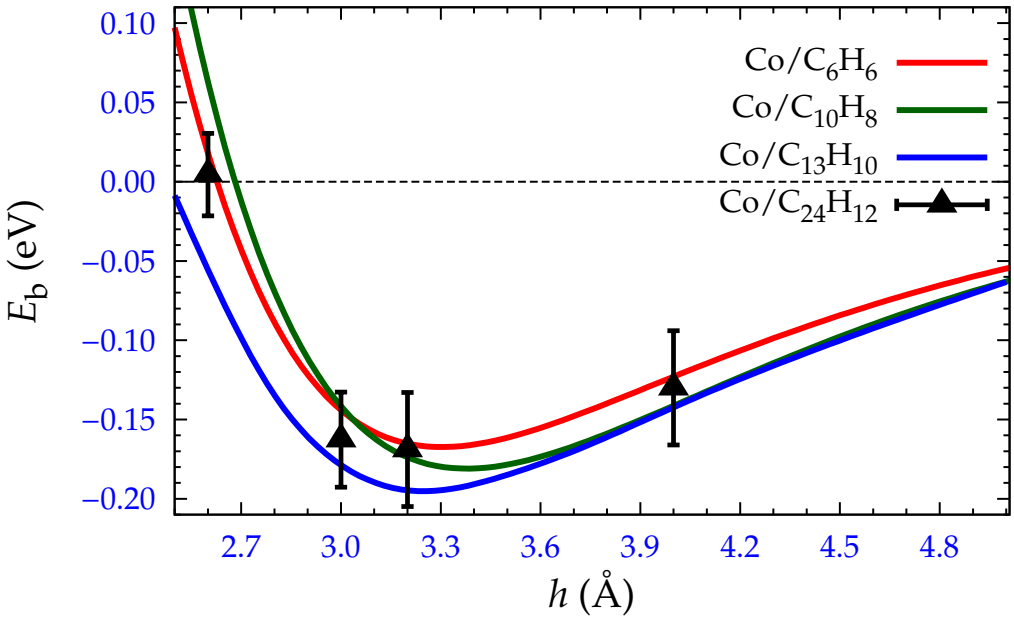

FIG. 5.10: Binding energies of Co/C_6H_6, $Co/C_{10}H_8$, $Co/C_{13}H_{10}$, and $Co/C_{24}H_{12}$ at the vdW region. The result for $Co/C_{24}H_{12}$ is obtained with AFQMC while the results for other clusters are provided by CCSD(T). Co, C, and H atoms use cc-pwCVQZ, cc-pVDZ, and cc-pVDZ basis sets, respectively. The CBS correction for this basis set is very small at this region.

5.5 Comparison with Experimental Results

A recent STM experiment for Co atoms on H-intercalated graphene/SiC(0001), also called quasi-free-standing monolayer graphene (QFMLG), reported that single Co atoms can be adsorbed at the top site and the hollow site with $h = 2.2$ Å and $h = 3.1$ Å, respectively [38]. The finding is in close agreement with our results. The vdW region in Fig. 5.9 can be associated with the hollow site, since any Co atoms in the vdW region at the top and bridge sites can easily hop to the top site global minimum due to low kinetic barriers, whereas Co atoms in the vdW hollow site cannot hop to the inner hollow site. The experiment also showed that Co atoms at the hollow site switched to the top site at a bias voltage of ~ -0.25 V, which is of the order of the vdW binding energy. This could allow Co atoms trapped at the hollow site vdW minimum to migrate to the top site.

Experimental studies of Co on graphene/SiC(0001), dubbed monolayer graphene (MLG), observed only the top site [37, 38], however. This difference might arise from the fact that MLG is less well modeled by the free graphene system studied here. MLG, grown on top of a carbon buffer layer, is strongly n-doped due to the interaction with the buffer layer, which can cause more deviations from the linear dispersion near the Dirac point [121, 122] than in QFMLG (which is only slightly p-doped [122, 123]). Furthermore, MLG shows significant corrugations, while QFMLG is exceptionally flat [122, 124].

Similar analysis may apply to STM experiments with Co on graphene/Pt(111), which observed only the hollow site at $h = 2.4$ Å [39]. Although the interaction of graphene and Pt(111) is assumed to be weak [125, 126], experimental studies suggest that there likely exists hybridization between graphene Dirac cone states and Pt d orbitals [127, 128]. A very similar situation was observed in STM experiments

for Co on graphene/Ir(111) which reported only the hollow site at $h = 2.7$ Å [42]. The interaction between graphene and Ir(111) is also assumed to be weak [129, 130]. However, experimental studies show that in-plane orientation of graphene on Ir(111) can significantly affect the electronic properties of graphene [131, 132]. Further investigations, both experimental and theoretical, are needed to resolve these issues and the substrate effects on graphene.

CHAPTER 6

Conclusion and Outlook

In summary, we have presented highly accurate *ab initio* many-body results on the adsorption of single Co adatoms on graphene for the three high-symmetry sites. We obtain exact results from free-projection AFQMC for the model systems Co/C_6H_6, Co/C_2H_4, and Co/C_4H_8 to benchmark DFT, with local and hybrid functionals, DFT+U, CCSD(T), and phaseless AFQMC. The benchmark studies show that phaseless AFQMC and CCSD(T) are essentially exact for high-spin Co configurations. However, for low-spin Co configurations, both phaseless AFQMC and CCSD(T) give small errors in binding energies. Further investigations are needed to improve accuracy, for example using multi-determinant trial/reference wavefunctions.

DFT with various functionals and DFT+U give widely varying results, cautioning that care must be taken in future studies of transition metal on graphene using such approaches. A quantitative measure of the accuracy is provided for the most commonly used functionals and for the choice of U values. None of the DFT functionals provides a uniformly correct description of all the three model systems.

The DFT+U results also show that there is no single correct value of U that can quantitatively describe all the model systems. These benchmark studies can assist in improving DFT functionals, and provide guidance for future studies of transition metal adsorption on graphene, especially in the selection of computationally less costly approaches.

A size-correction embedding scheme is employed to calculate the binding energy of Co/graphene. We show that the size-correction method is insensitive to the choice of DFT exchange-correlation functional, even though the different functionals differ in their description of the components. Our tests show that, to reach the desired accuracy in predicting the binding energies in Co/graphene, the three model systems are inadequate to be used as the near regions for an embedding treatment. Instead we use Co/$C_{24}H_{12}$, Co/$C_{10}H_8$, and Co/$C_{13}H_{10}$ as the near regions for the hollow, the bridge, and the top sites, respectively. The finite-size corrections are relatively small for these large clusters.

We next use frozen-orbital phaseless AFQMC to perform direct many-body calculations on these large clusters. We obtain the binding energy of Co/graphene after applying the size-correction embedding scheme. We find that the Co atom can be adsorbed at the top site with $E_\mathrm{b} \sim -0.31\,\mathrm{eV}$ and at the vdW region with $E_\mathrm{b} \sim -0.18\,\mathrm{eV}$. Although the bridge and the hollow sites are bound, they are either metastable or inaccessible in the adsorption process. The results explain recent experimental observations for Co on H-intercalated graphene/SiC(0001).

In this study, we use a pure graphene for Co/graphene system. While in real experiments, graphene is usually supported by a substrate. Experimental studies show that the substrate of graphene can play an important role in Co adsorption on graphene as discussed below.

6.1 The Role of Substrate in Co/graphene

H-intercalated graphene/SiC(0001), also called quasi-free-standing monolayer graphene (QFMLG) is very well modeled by the free graphene system studied here since it is exceptionally flat [122, 124] and only slightly p doped [122, 123]. Thus our results are expected to be in agreement with the STM experiment for Co on QFMLG. Interestingly, the graphene substrate can highly affect the properties of Co/graphene. For example, without hydrogen intercalation, the STM experiment for Co on graphene/SiC(0001) observed only the top site.

Metal substrates for Co/graphene even offers the ability to tailor the magnetism of Co atoms on graphene [39, 41, 42]. Cobalt atoms on graphene/Ru(0001), due to a strong interaction between graphene and Ru, feature remarkably large orbital and spin moments with an out-of-plane easy axis, as well as large magnetic anisotropy. On the contrary, the magnetic moments of Co atoms on graphene/Ir(111) are strongly reduced and the magnetization is of the easy-plane axis. The preferred magnetization direction for Co on graphene/Pt(111) lies in plane, similar to that of Co/graphene/Ir(111), however, it also shows large magnetic anisotropy.

The Ru(0001) substrate is also known to cause graphene to ripple, creating a moiré pattern [133]. STM experiments reveal that the Co atoms can be adsorbed at the moiré valleys and moiré hills [41, 42]. The experiments further show that the Co atoms at the moiré hills exhibit Kondo features. The Kondo resonance disappears, however, as the graphene is flattened by silicon intercalation [41], which indicates that the ripples in graphene are the key to have the Kondo effect.

Further studies of the substrate effects on Co/graphene would be worthwhile and could be a future project.

BIBLIOGRAPHY

[1] P. R. Wallace, Phys. Rev. **71**, 622 (1947).

[2] A. K. Geim and K. S. Novoselov, Nat. Mater. **6**, 183 (2007).

[3] K. S. Novoselov, A. K. Geim, S. V. Morozov, D. Jiang, Y. Zhang, S. V. Dubonos, I. V. Grigorieva, and A. A. Firsov, Science **306**, 666 (2004).

[4] A. H. Castro Neto, F. Guinea, N. M. R. Peres, K. S. Novoselov, and A. K. Geim, Rev. Mod. Phys. **81**, 109 (2009).

[5] K. S. Novoselov, V. I. Fal'ko, L. Colombo, P. R. Gellert, M. G. Schwab, and K. Kim, Nature **490**, 192 (2012).

[6] C. Lee, X. Wei, J. W. Kysar, and J. Hone, Science **321**, 385 (2008).

[7] A. Akturk and N. Goldsman, J. Appl. Phys. **103**, 053702 (2008).

[8] K. Bolotin, K. Sikes, Z. Jiang, M. Klima, G. Fudenberg, J. Hone, P. Kim, and H. Stormer, Solid State Commun. **146**, 351 (2008).

[9] A. K. Geim, Science **324**, 1530 (2009).

[10] O. V. Yazyev, Rep. Prog. Phys. **73**, 056501 (2010).

[11] Q. Zhang, K. S. Chan, and Z. Lin, Appl. Phys. Lett. **98**, 032106 (2011).

[12] D. Pesin and A. H. MacDonald, Nat. Mater. **11**, 409 (2012).

[13] V. N. Kotov, B. Uchoa, V. M. Pereira, F. Guinea, and A. H. Castro Neto, Rev. Mod. Phys. **84**, 1067 (2012).

[14] S. Murakami, N. Nagaosa, and S.-C. Zhang, Science **301**, 1348 (2003).

[15] I. Žutić, J. Fabian, and S. Das Sarma, Rev. Mod. Phys. **76**, 323 (2004).

[16] O. V. Yazyev and L. Helm, Phys. Rev. B **75**, 125408 (2007).

[17] R. R. Nair, M. Sepioni, I.-L. Tsai, O. Lehtinen, J. Keinonen, A. V. Krasheninnikov, T. Thomson, A. K. Geim, and I. V. Grigorieva, Nat Phys **8**, 199 (2012).

[18] G. Z. Magda, X. Jin, I. Hagymasi, P. Vancso, Z. Osvath, P. Nemes-Incze, C. Hwang, L. P. Biro, and L. Tapaszto, Nature **514**, 608 (2014).

[19] Y. Yagi, T. M. Briere, M. H. F. Sluiter, V. Kumar, A. A. Farajian, and Y. Kawazoe, Phys. Rev. B **69**, 075414 (2004).

[20] Y. Mao, J. Yuan, and J. Zhong, J. Phys.: Condens. Matter **20**, 115209 (2008).

[21] H. Johll, H. C. Kang, and E. S. Tok, Phys. Rev. B **79**, 245416 (2009).

[22] T. O. Wehling, H. P. Dahal, A. I. Lichtenstein, M. I. Katsnelson, H. C. Manoharan, and A. V. Balatsky, Phys. Rev. B **81**, 085413 (2010).

[23] T. O. Wehling, A. V. Balatsky, M. I. Katsnelson, A. I. Lichtenstein, and A. Rosch, Phys. Rev. B **81**, 115427 (2010).

[24] D. Jacob and G. Kotliar, Phys. Rev. B **82**, 085423 (2010).

[25] C. Cao, M. Wu, J. Jiang, and H.-P. Cheng, Phys. Rev. B **81**, 205424 (2010).

[26] H. Valencia, A. Gil, and G. Frapper, J. Phys. Chem. C **114**, 14141 (2010).

[27] K. T. Chan, H. Lee, and M. L. Cohen, Phys. Rev. B **83**, 035405 (2011).

[28] X. Liu, C. Z. Wang, Y. X. Yao, W. C. Lu, M. Hupalo, M. C. Tringides, and K. M. Ho, Phys. Rev. B **83**, 235411 (2011).

[29] M. Sargolzaei and F. Gudarzi, J. Appl. Phys. **110**, 064303 (2011).

[30] J. Ding, Z. Qiao, W. Feng, Y. Yao, and Q. Niu, Phys. Rev. B **84**, 195444 (2011).

[31] T. O. Wehling, A. I. Lichtenstein, and M. I. Katsnelson, Phys. Rev. B **84**, 235110 (2011).

[32] A. N. Rudenko, F. J. Keil, M. I. Katsnelson, and A. I. Lichtenstein, Phys. Rev. B **86**, 075422 (2012).

[33] Y. Virgus, W. Purwanto, H. Krakauer, and S. Zhang, Phys. Rev. B **86**, 241406(R) (2012).

[34] Y. Virgus, W. Purwanto, H. Krakauer, and S. Zhang, Phys. Rev. Lett. **113**, 175502 (2014).

[35] V. W. Brar, R. Decker, H.-M. Solowan, Y. Wang, L. Maserati, K. T. Chan, H. Lee, C. O. Girit, A. Zettl, S. G. Louie, et al., Nat. Phys. **7**, 43 (2011).

[36] Y. Wang, V. W. Brar, A. V. Shytov, Q. Wu, W. Regan, H.-Z. Tsai, A. Zettl, L. S. Levitov, and M. F. Crommie, Nat. Phys. **8**, 653 (2012).

[37] T. Eelbo, M. Waśniowska, P. Thakur, M. Gyamfi, B. Sachs, T. O. Wehling, S. Forti, U. Starke, C. Tieg, A. I. Lichtenstein, et al., Phys. Rev. Lett. **110**, 136804 (2013).

[38] T. Eelbo, M. Waśniowska, M. Gyamfi, S. Forti, U. Starke, and R. Wiesendanger, Phys. Rev. B **87**, 205443 (2013).

[39] F. Donati, Q. Dubout, G. Autès, F. Patthey, F. Calleja, P. Gambardella, O. V. Yazyev, and H. Brune, Phys. Rev. Lett. **111**, 236801 (2013).

[40] V. Sessi, S. Stepanow, A. N. Rudenko, S. Krotzky, K. Kern, F. Hiebel, P. Mallet, J.-Y. Veuillen, O. Šipr, J. Honolka, et al., New J. Phys. **16**, 062001 (2014).

[41] J. Ren, H. Guo, J. Pan, Y. Y. Zhang, X. Wu, H.-G. Luo, S. Du, S. T. Pantelides, and H.-J. Gao, Nano Lett. **14**, 4011 (2014).

[42] F. Donati, L. Gragnaniello, A. Cavallin, F. D. Natterer, Q. Dubout, M. Pivetta, F. Patthey, J. Dreiser, C. Piamonteze, S. Rusponi, et al., Phys. Rev. Lett. **113**, 177201 (2014).

[43] J. P. Perdew, K. Burke, and M. Ernzerhof, Phys. Rev. Lett. **77**, 3865 (1996).

[44] A. D. Becke, J. Chem. Phys. **98**, 5648 (1993).

[45] A. I. Lichtenstein and M. I. Katsnelson, Phys. Rev. B **57**, 6884 (1998).

[46] M. Cococcioni and S. de Gironcoli, Phys. Rev. B **71**, 035105 (2005).

[47] B. Roos, Chem. Phys. Lett. **15**, 153 (1972).

[48] S. Zhang, J. Carlson, and J. E. Gubernatis, Phys. Rev. B **55**, 7464 (1997).

[49] S. Zhang and H. Krakauer, Phys. Rev. Lett. **90**, 136401 (2003).

[50] S. Zhang, in *Emergent Phenomena in Correlated Matter*, edited by E. Pavarini, E. Koch, and U. Schollwöck (Forschungszentrum Jülich Zentralbibliothek, Verlag, 2013), chap. 15.

[51] R. M. Martin, *Electronic Structure: Basic Theory and Practical Methods* (Cambridge University Press, 2004).

[52] L. Kantorovich, *Quantum Theory of the Solid State: An Introduction* (Kluwer Academic Publisher, 2004).

[53] P. Hohenberg and W. Kohn, Phys. Rev. **136**, B864 (1964).

[54] W. Kohn and L. J. Sham, Phys. Rev. **140**, A1133 (1965).

[55] D. M. Ceperley and B. J. Alder, Phys. Rev. Lett. **45**, 566 (1980).

[56] J. P. Perdew and A. Zunger, Phys. Rev. B **23**, 5048 (1981).

[57] K. Burke, J. Chem. Phys. **136**, 150901 (2012).

[58] A. Szabo and N. S. Ostlund, *Modern Quantum Chemistry: Introduction to Advanced Electronic Structure Theory* (Dover Publications, 1996).

[59] F. Jensen, *Introduction to Computational Chemistry* (John Wiley & Sons, 2007).

[60] R. J. Bartlett and M. Musiał, Rev. Mod. Phys. **79**, 291 (2007).

[61] T. D. Crawford and H. F. Schaefer, *An Introduction to Coupled Cluster Theory for Computational Chemists* (John Wiley & Sons, Inc., 2007), pp. 33–136.

[62] R. J. Bartlett, WIREs Comput. Mol. Sci. **2**, 126 (2012).

[63] W. M. C. Foulkes, L. Mitas, R. J. Needs, and G. Rajagopal, Rev. Mod. Phys. **73**, 33 (2001).

[64] J. Kolorenč and L. Mitas, Reports on Progress in Physics **74**, 026502 (2011).

[65] P. J. Reynolds, D. M. Ceperley, B. J. Alder, and W. A. Lester, J. Chem. Phys. **77**, 5593 (1982).

[66] B. L. Hammond, W. A. Lester, and P. J. Reynolds, *Monte Carlo Methods in Ab Initio Quantum Chemistry* (World Scientific, 1994).

[67] W. Purwanto and S. Zhang, Phys. Rev. E **70**, 056702 (2004).

[68] W. Purwanto and S. Zhang, Phys. Rev. A **72**, 053610 (2005).

[69] W. A. Al-Saidi, H. Krakauer, and S. Zhang, Phys. Rev. B **73**, 075103 (2006).

[70] W. A. Al-Saidi, S. Zhang, and H. Krakauer, J. Chem. Phys. **124**, 224101 (2006).

[71] W. A. Al-Saidi, H. Krakauer, and S. Zhang, J. Chem. Phys. **125**, 154110 (2006).

[72] W. A. Al-Saidi, H. Krakauer, and S. Zhang, J. Chem. Phys. **126**, 194105 (2007).

[73] W. A. Al-Saidi, S. Zhang, and H. Krakauer, J. Chem. Phys. **127**, 144101 (2007).

[74] M. Suewattana, W. Purwanto, S. Zhang, H. Krakauer, and E. J. Walter, Phys. Rev. B **75**, 245123 (2007).

[75] W. Purwanto, W. A. Al-Saidi, H. Krakauer, and S. Zhang, J. Chem. Phys. **128**, 114309 (2008).

[76] W. Purwanto, S. Zhang, and H. Krakauer, J. Chem. Phys. **130**, 094107 (2009).

[77] W. Purwanto, H. Krakauer, and S. Zhang, Phys. Rev. B **80**, 214116 (2009).

[78] W. Purwanto, H. Krakauer, Y. Virgus, and S. Zhang, J. Chem. Phys. **135**, 164105 (2011).

[79] F. Ma, S. Zhang, and H. Krakauer, New J. Phys. **15**, 093017 (2013).

[80] H. Shi and S. Zhang, Phys. Rev. B **88**, 125132 (2013).

[81] C.-C. Chang and S. Zhang, Phys. Rev. B **78**, 165101 (2008).

[82] C.-C. Chang and S. Zhang, Phys. Rev. Lett. **104**, 116402 (2010).

[83] W. Purwanto, S. Zhang, and H. Krakauer, J. Chem. Theory Comput. **9**, 4825 (2013).

[84] J. W. Negele and H. Orland, *Quantum Many-Particle Systems* (Perseus Books, 1998).

[85] A. Fetter and J. Walecka, *Quantum theory of Many-Particle Systems* (Dover Publications, 2003).

[86] H. F. Trotter, Proc. Am. Math. Soc. **10**, 545 (1959).

[87] M. Suzuki, Commun. Math. Phys. **51**, 183 (1976).

[88] R. D. Stratonovich, Dokl. Akad. Nauk. SSSR **115**, 1907 (1957).

[89] J. Hubbard, Phys. Rev. Lett. **3**, 77 (1959).

[90] M. Svensson, S. Humbel, R. D. J. Froese, T. Matsubara, S. Sieber, and K. Morokuma, J. Phys. Chem. **100**, 19357 (1996).

[91] N. Govind, Y. A. Wang, and E. A. Carter, J. Chem. Phys. **110**, 7677 (1999).

[92] P. Huang and E. A. Carter, J. Chem. Phys. **125**, 084102 (2006).

[93] P. Huang and E. A. Carter, Annu. Rev. Phys. Chem. **59**, 261 (2008), also see the references therein.

[94] P. Elliott, K. Burke, M. H. Cohen, and A. Wasserman, Phys. Rev. A **82**, 024501 (2010).

[95] J. M. Foster and S. F. Boys, Rev. Mod. Phys. **32**, 300 (1960).

[96] G. H. Wannier, Phys. Rev. **52**, 191 (1937).

[97] N. Marzari and D. Vanderbilt, Phys. Rev. B **56**, 12847 (1997).

[98] M. Valiev, E. J. Bylaska, N. Govind, K. Kowalski, T. P. Straatsma, H. J. J. Van Dam, D. Wang, J. Nieplocha, E. Apra, T. L. Windus, et al., Comput. Phys. Commun. **181**, 1477 (2010).

[99] N. H. F. Beebe and J. Linderberg, Int. J. Quant. Chem. **12**, 683 (1977).

[100] H. Koch, A. S. de Merás, and T. B. Pedersen, J. Chem. Phys. **118**, 9481 (2003).

[101] F. Aquilante, L. D. Vico, N. Ferré, G. Ghigo, P. Å. Malmqvist, P. Neogrády, T. B. Pedersen, M. Pitoňák, M. Reiher, B. O. Roos, et al., J. Comput. Chem. **31**, 224 (2010).

[102] G. Moore, Proceedings of the IEEE **86**, 82 (1998).

[103] R. Keyes, Rep. Prog. Phys. **68**, 2701 (2005).

[104] F. Schwierz, Nat. Nanotechnol. **5**, 487 (2010).

[105] M. Sprinkle, M. Ruan, Y. Hu, J. Hankinson, M. Rubio-Roy, B. Zhang, X. Wu, C. Berger, and W. A. de Heer, Nat. Nanotechnol. **5**, 727 (2010).

[106] B. Uchoa, T. G. Rappoport, and A. H. Castro Neto, Phys. Rev. Lett. **106**, 016801 (2011).

[107] L. Li, Y.-Y. Ni, Y. Zhong, T.-F. Fang, and H.-G. Luo, New J. Phys. **15**, 053018 (2013).

[108] P. Giannozzi, S. Baroni, N. Bonini, M. Calandra, R. Car, C. Cavazzoni, D. Ceresoli, G. L. Chiarotti, M. Cococcioni, I. Dabo, et al., J. Phys.: Condens. Matter **21**, 395502 (2009).

[109] T. Helgaker, W. Klopper, H. Koch, and J. Noga, J. Chem. Phys. **106**, 9639 (1997).

[110] D. Feller, J. Chem. Phys. **98**, 7059 (1993).

[111] A. Halkier, T. Helgaker, P. Jorgensen, W. Klopper, and J. Olsen, Chem. Phys. Lett. **302**, 437 (1999).

[112] C. Adamo and V. Barone, J. Chem. Phys. **110**, 6158 (1999).

[113] J. Heyd, G. E. Scuseria, and M. Ernzerhof, J. Chem. Phys. **118**, 8207 (2003).

[114] J. Heyd, G. E. Scuseria, and M. Ernzerhof, J. Chem. Phys. **124**, 219906 (2006).

[115] M. Caricato, T. Vreven, G. W. Trucks, and M. J. Frisch, J. Chem. Phys. **133**, 054104 (2010).

[116] P. M. Morse, Phys. Rev. **34**, 57 (1929).

[117] K. Berland, C. A. Arter, V. R. Cooper, K. Lee, B. I. Lundqvist, E. Schröder, T. Thonhauser, and P. Hyldgaard, J. Chem. Phys. **140**, 18A539 (2014).

[118] J. Klimes and A. Michaelides, J. Chem. Phys. **137**, 120901 (2012).

[119] H. Rydberg, M. Dion, N. Jacobson, E. Schröder, P. Hyldgaard, S. I. Simak, D. C. Langreth, and B. I. Lundqvist, Phys. Rev. Lett. **91**, 126402 (2003).

[120] M. Dion, H. Rydberg, E. Schröder, D. C. Langreth, and B. I. Lundqvist, Phys. Rev. Lett. **92**, 246401 (2004).

[121] Y. Qi, S. H. Rhim, G. F. Sun, M. Weinert, and L. Li, Phys. Rev. Lett. **105**, 085502 (2010).

[122] S. Forti, K. V. Emtsev, C. Coletti, A. A. Zakharov, C. Riedl, and U. Starke, Phys. Rev. B **84**, 125449 (2011).

[123] C. Riedl, C. Coletti, T. Iwasaki, A. A. Zakharov, and U. Starke, Phys. Rev. Lett. **103**, 246804 (2009).

[124] S. Goler, C. Coletti, V. Piazza, P. Pingue, F. Colangelo, V. Pellegrini, K. V. Emtsev, S. Forti, U. Starke, F. Beltram, et al., Carbon **51**, 249 (2013).

[125] A. B. Preobrajenski, M. L. Ng, A. S. Vinogradov, and N. Mårtensson, Phys. Rev. B **78**, 073401 (2008).

[126] P. Sutter, J. T. Sadowski, and E. Sutter, Phys. Rev. B **80**, 245411 (2009).

[127] S. Rajasekaran, S. Kaya, T. Anniyev, H. Ogasawara, and A. Nilsson, Phys. Rev. B **85**, 045419 (2012).

[128] Q. Zhou, S. Coh, M. L. Cohen, S. G. Louie, and A. Zettl, Phys. Rev. B **88**, 235431 (2013).

[129] I. Pletikosić, M. Kralj, P. Pervan, R. Brako, J. Coraux, A. T. N'Diaye, C. Busse, and T. Michely, Phys. Rev. Lett. **102**, 056808 (2009).

[130] C. Busse, P. Lazić, R. Djemour, J. Coraux, T. Gerber, N. Atodiresei, V. Caciuc, R. Brako, A. T. N'Diaye, S. Blügel, et al., Phys. Rev. Lett. **107**, 036101 (2011).

[131] E. Starodub, A. Bostwick, L. Moreschini, S. Nie, F. E. Gabaly, K. F. McCarty, and E. Rotenberg, Phys. Rev. B **83**, 125428 (2011).

[132] D. Marchenko, J. Sánchez-Barriga, M. R. Scholz, O. Rader, and A. Varykhalov, Phys. Rev. B **87**, 115426 (2013).

[133] W. Moritz, B. Wang, M.-L. Bocquet, T. Brugger, T. Greber, J. Wintterlin, and S. Günther, Phys. Rev. Lett. **104**, 136102 (2010).

VITA

Yudistira Virgus

Yudistira Virgus was born on August 28, 1985 in Palembang, South Sumatra, Indonesia. In 2004, he represented Indonesia in the XXXV International Physics Olympiad in Pohang, Korea and won a gold medal. In the same year, he pursued his interest in science by studying physics at the Institut Teknologi Bandung, in Bandung, West Java, Indonesia. He graduated with Cum Laude honors in July 2008. He entered College of William and Mary in Williamsburg, Virginia in Fall 2009 to study in the physics graduate program. In the fall of 2010, he joined Dr. Henry Krakauer and Dr. Shiwei Zhang's computational condensed matter physics group. He defended his thesis on May 8, 2015.